

REVISION 1

Ferro-tschermakite with polysomatic chain-width disorder identified in silician magnetite from Wirrda Well, South Australia: a HAADF STEM study

CRISTIANA L. CIOBANU^{1,*}, MAX R. VERDUGO-IHL¹, NIGEL J. COOK², KATHY EHRIG^{2,3},

ASHLEY SLATTERY⁴, LIAM COURTNEY-DAVIES¹

¹ School of Chemical Engineering and Advanced Materials, The University of Adelaide, Adelaide, SA,
5000, Australia

² School of Civil, Environmental and Mining Engineering, The University of Adelaide, Adelaide, SA,
5000, Australia

³ BHP Olympic Dam, 10 Franklin St., Adelaide, South Australia 5000, Australia

⁴ Adelaide Microscopy, The University of Adelaide, Adelaide, SA, 5000, Australia

ABSTRACT

Silician magnetite within ~1.85 Ga lithologies hosting the ~1.6 Ga Wirrda Well iron oxide copper gold (IOCG) prospect, South Australia, was examined at the nanoscale. The magnetite is oscillatory-zoned with respect to the density and orientation of nm-scale inclusions, among which Si-Fe-nanorods and Al-rich amphibole (as much as hundreds of nm long and tens of nm wide) form swarms along $\langle 111 \rangle$ directions in magnetite. The amphibole is identified as ferro-tschermakite (Ftsk) with the crystal-chemical formula: $A(K_{0.06}Na_{0.01})_{0.07}B(Ca_{1.65}Na_{0.35})_2C(Fe^{2+}_{2.07}Al_{1.64}Mg_{1.15}Ti_{0.06}Fe^{3+}_{0.04}Mn_{0.04})_5T(Si_{6.48}Al_{1.52})_8O_{22}^W(OH)_2$. This contains single and double rows of a triple-chain silicate attributed to clinojimthompsonite (Cjt), as coherently intergrown (010) zippers along the entire length of the grains. High-angle annular dark field scanning transmission electron microscopy (HAADF STEM) imaging and simulation of Ftsk and Cjt on the [001] zone axis provide direct visualization of crystal structures. These are defined by the 7- and 10-atom octahedron strips ($B+C$ sites) and flanked by double- and triple-pairs

*Corresponding author. E-mail address: cristiana.ciobanu@adelaide.edu.au

Always consult and cite the final, published document. See <http://www.minsocam.org> or GeoscienceWorld

24 of Si atoms (*T* sites). Remarkably, the sites for light cations and/or vacancies are clearly imaged as single
25 and double, darkest, diamond-shaped motifs separating the octahedron strips showing that *A* cavities
26 known in amphibole are readily depicted in the wider-chain silicate. *I-beam* models show that nanoscale
27 intergrowths among the two silicates are coherent along zig-zag chains of cations at the edges of the
28 octahedron strips, with single and double rows of the triple-chain silicate corresponding to 1- and 1.5-
29 unit cells of Cjt (27 and 41 Å intervals along the *b* axis). This type of polysomatic chain-width disorder
30 is widely reported in Mg-rich pyriboles but is shown here in an Al-Fe-rich amphibole. The lack of planar
31 defects and/or reaction fronts at mutual contacts between 3-chain zippers and host amphibole indicates
32 primary co-crystallization growth, promoted by formation of the Si-Fe-nanorods. Co-crystallizing
33 plagioclase is also preserved in close vicinity to the amphibole hosted by magnetite (from a few nm to
34 μm apart). In contrast, replacement of amphibole by phyllosilicates is recognizable as irregular swells
35 along the (010) zippers and results in extensive chloritization of the amphibole during an overprinting
36 event. Pressures of ~11.5 kbar are estimated using Al-in-hornblende nano-geobarometry and calculated
37 Al content in Ftsk (3.16 a.p.f.u.). Assuming the amphibole-plagioclase association buffered by host
38 magnetite fulfils the textural equilibration criteria required for application of this barometer, we interpret
39 the Ftsk nanoinclusions in magnetite as preserved evidence for amphibolite facies metamorphism
40 affecting host lithologies at Wirrda Well with subsequent retrograde alteration during the ~1.6 Ga IOCG
41 mineralizing event. Magnetite records petrogenetic processes by accommodating variable ranges of
42 nanomineral inclusions and preserving them over geological time scales. HAADF STEM imaging is
43 ideally suited to depiction of crystal-structural modularity and also provides insights into the evolution
44 of geological terranes with protracted histories.

45 **Keywords:** silician magnetite, ferro-tschermakite, clinojimthompsonite, polysomatic chain-width
46 disorder, pyriboles, HAADF STEM

47

INTRODUCTION

48 Scanning Transmission Electron Microscopy (STEM) using a High Angle Annular Dark Field
49 (HAADF) detector provides sub-Ångstrom atomic-scale resolution when combined with contemporary
50 instruments offering improved aberration-correction of the probe forming optics (e.g., van Tendeloo et
51 al. 2012). One of the main advantages of using HAADF STEM over High Resolution (HR) TEM
52 techniques is that the image is formed from a convergent rather than parallel beam (Van Tendeloo et al.
53 2012) and thus, the displayed ‘dots’ are directly attributable to atoms, with a distribution that is unaffected
54 by focus and thickness as in conventional HR TEM imaging. This enables an unparalleled route to direct
55 imaging of minerals and their intergrowths at the nanoscale, in turn providing insights into petrological
56 processes that cannot be constrained by other methods (Ciobanu et al. 2019a, and references therein). In
57 HAADF STEM mode, the image contrast is correlated with atomic mass, i.e., the atomic number Z -
58 dependence of the contrast is $\sim Z^2$, with application to the smallest U-bearing nanoparticles in
59 environmental studies (e.g., Utsunomiya and Ewing 2003). Recent HAADF STEM studies of Pb-Bi
60 sulfosalts, REE-fluorocarbonates, and Pb-Bi- or Bi-chalcogenides show how we can directly visualize
61 structural blocks defining the homology of a mineral series and layer types in mixed-layer compounds
62 (Medlin et al. 2010, 2013, 2014, 2019; Ciobanu et al. 2016, 2017; Li et al. 2019; Cook et al. 2019).

63 Crystal-structural modularity is a concept widely used in modern mineral classification schemes,
64 including those based on the topology of SiO_4 tetrahedral groups (T) defining the major categories of
65 rock-forming silicates (Deer et al. 2013). Among these, biopyriboles form a group that combine T -sheet
66 and -chain silicates and have been used to define polysomatism and its application to derive modular
67 series (e.g., Thompson 1978; Veblen 1981). Of interest here are the pyriboles which comprise only chain
68 silicates, in which the number of chains (n) defines pyroxenes ($n=1$), amphiboles ($n=2$) and non-classical
69 pyriboles (NCP) with $n>2$, as well as those with two or more different chains in combinations (Veblen
70 et al. 1977; Veblen and Burnham 1978a, b; Veblen and Buseck 1979, 1980). Pyriboles are well-known

71 for their ability to form coherent lattice-scale intergrowths with one another, also called polysomatic
72 intergrowths, as shown by many HR TEM studies of natural or synthetic material (e.g., Veblen 1992;
73 Veblen et al. 1993; Bozhilov 2013, and references therein).

74 To date, none of the studies addressing complex pyribole sequences, their degree of order and
75 disorder, or the diverse range of defects present (stacking faults, dislocations, chain terminations, etc.)
76 has been carried out using HAADF STEM imaging. Using this technique, we identify ferro-tschermakite
77 occurring as nanoinclusions in magnetite. We show the advantages of such an approach to the direct
78 visualization of the building blocks that define their crystal-structural modularity and the presence of
79 polysomatic disorder as lamellar intergrowths with NCP layers.

80 Mineral inclusions in magnetite are increasingly reported from nanoscale studies using Z-contrast
81 STEM imaging techniques of minerals from deposits spanning the magmatic-hydrothermal spectrum (Xu
82 et al. 2014; Deditius et al. 2018; Ciobanu et al. 2019b; Gao et al. 2019a, b; Yin et al. 2019; Verdugo Ihl
83 et al. 2021). Whereas crystallographically-oriented inclusions of magnetite are common in pyroxenes
84 from igneous and metamorphic rocks (Fleet et al. 1980), inclusions of magnetite in amphibole, or vice-
85 versa, are largely unreported.

86 Silician magnetite, known from many deposit types, can accommodate vacancy-bearing Si-Fe-
87 nanoprecipitates with widths of multiple d_{111} magnetite, as shown for banded iron formation (BIF) and
88 iron-oxide copper gold (IOCG) deposits (Xu et al. 2014; and review of silician magnetite in Ciobanu et
89 al. 2019b). In the outer shell from the ~1.6 Ga IOCG deposit at Olympic Dam (South Australia), silician
90 magnetite contains abundant nanoscale inclusions of (ferro)actinolite, one of several calc-silicates
91 formed during alkali-calcic alteration of host granite (Ciobanu et al. 2019; Verdugo-Ihl et al. 2020a).
92 Based on trace element geochemistry, silician magnetite is also known from the Cu-(Au) prospect at
93 Wirrda Well, also within the Olympic Dam district where mineralization belongs to the same ~1.6 Ga
94 IOCG event defining the Olympic Cu-Au Province (1598.9 ± 6.3 Ma $^{207}\text{Pb}/^{206}\text{Pb}$ age obtained from U-

95 bearing hematite; Courtney-Davies et al. 2019). The Wirrda Well prospect is, however, hosted by an
96 older, ~1.85 Ga granite (Donington Suite; DS) that experienced burial metamorphism at conditions from
97 granulite to greenschist facies during the 1735–1690 Ma Kimban orogeny (Reid 2019, and references
98 therein). Numerous mafic dikes, some of which are penecontemporaneous with the DS suite, as well as
99 shear zones, are typical of the geological setting at Wirrda Well (e.g., Courtney-Davies et al. 2019).

100 The present HAADF STEM study addresses amphibole and other nm-scale mineral inclusions in
101 silician magnetite from Wirrda Well. The aim is to understand the petrogenetic significance of such
102 nanoscale inclusions in the context of protracted igneous-metamorphic history. Comparison with
103 magnetite from other deposits/prospects in the district constrains mineral signatures recorded during the
104 early stages of IOCG systems.

105 BACKGROUND ON TSCHERMAKITE AND PYRIBOLES

106 Amphiboles are a large group of inosilicates with the general formula: $AB_2C_5T_8O_{22}W_2$, where A =
107 vacancy (\square), Na, K, Ca, Pb, Li; B = Na, Ca, Mn^{2+} , Fe^{2+} , Mg, Li; C = Mg, Fe^{2+} , Mn^{2+} , Al, Fe^{3+} , Mn^{3+} ,
108 Ti^{4+} , Li; T = Si, Al, Ti^{4+} , Be; and W = (OH), F, Cl, O^{2-} (Hawthorne et al. 2012). Of these, the Al-rich,
109 calcic amphiboles with $C2/m$ symmetry comprising the solid solution series between the Mg-endmember
110 tschermakite: $A_{\square}B_{\square}Ca_2C(Mg_3Al_2)^T(Si_6Al_2)O_{22}W(OH)_2$ (Abdu and Hawthorne 2009) and Fe-endmember
111 ferro-tschermakite, $A_{\square}B_{\square}Ca_2C(Fe^{2+}_3Al_2)^T(Si_6Al_2)O_{22}W(OH)_2$ (Hawthorne and Grundy 1978; Oberti et al.
112 2018) are rare species documented only from a limited number of localities.

113 The tschermakite crystal structure was refined from a specimen at the contact between anorthosite and
114 amphibolite from Fiskenaasset, Greenland (Abdu and Hawthorne 2009; Table 1). However, Oberti et al.
115 (2018) discredited the Fiskenaasset specimen as being a magnesiohornblende variety, based on
116 redefinition of tschermakite within a narrower compositional field: $1.5 <^C(Al+Fe^{3+}+2Ti) < 2$ a.p.f.u and
117 $0 <^A(Na+K+2Ca) < 0.5$ a.p.f.u (Hawthorne et al. 2012). The ferro-tschermakite crystal structure was
118 refined by Hawthorne and Grundy (1973) and the formal description of the mineral given by Oberti et

119 al. (2018) from a specimen in the Ploumanac'h granitic complex, France (Table 1).

120 When projected along the c axis, the basic amphibole structure (Fig. 1a) can be visualized as two
121 double-chains of SiO_4 tetrahedra [$T(1)$ and $T(2)$] sandwiching an octahedron strip of C -group cations
122 [$M(1)$, $M(2)$ and $M(3)$], collectively making up what is known as an I -beam stack, two chains in width
123 (Papike and Ross 1970). The B -group cations occupy the $M(4)$ site and link the octahedron strip to the
124 tetrahedron double chain, whereas the A -group cations occupy the A cavity with several distinct sites of
125 which only the $A(m)$ and $A(2)$ sites are occupied (Hawthorne et al. 2005, and references therein). These
126 authors discuss order and disorder phenomena in amphiboles in terms of site occupancy, whereby Short-
127 Range Order (SRO) is defined as local clusters of atoms, either in excess or deficit, over a single site. Of
128 interest here are the A sites that can be depicted by HAADF STEM imaging since these contain light
129 cations (\pm vacancies) thus contrasting with the cations filling the other sites defining the I -beam stacks in
130 the structure.

131 Aside from pyroxenes and amphiboles (1- and 2-chains wide, respectively), NCP pyriboles include
132 those with triple chains of I -beams (jimthompsonite and clinojimthompsonite) and alternating double
133 and triple chains (chesterite) identified in metamorphic rocks from Chester, Vermont (Veblen and
134 Burnham 1978). Of interest here is clinojimthompsonite with the ideal formula: $\text{Oct}(\text{Mg},$
135 $\text{Fe})_{10}\text{Tet}\text{Si}_{12}\text{O}_{32}(\text{OH})_4$ (Oct=octahedral; Tet=tetrahedral), described as a Mg-Fe-rich variety from the type
136 locality: $\text{Na}_{0.04}\text{Oct}(\text{Mg}_{7.59}\text{Fe}^{2+}_{2.07}\text{Mn}_{0.13}\text{Ca}_{0.11})_{\Sigma 9.95}\text{Tet}(\text{Si}_{11.97}\text{Al}_{0.07})_{\Sigma 12}\text{O}_{32}(\text{OH})_4$ (Veblen and Burnham 1978;
137 Fig. 1b). A calcic analogue of clinojimthompsonite: $\text{K}_{0.054}\text{Na}_{0.029}(\text{Mg}_{7.783}\text{Ca}_{1.958}\text{Fe}^{2+}_{0.222}\text{Mn}_{0.014})_{\Sigma 9.977}$
138 $(\text{Si}_{11.970}\text{Al}_{0.028})_{\Sigma 11.998}\text{O}_{32}(\text{OH})_4$ was identified from Oeyama ophiolite, Japan (Konishi et al. 1993).

139 Modularity in pyriboles has been conceptualised by defining two main building blocks: mica (**M**) and
140 pyroxene (**p**), each with a dimension of ~ 4.5 Å along the b axis, so that the structures can be visualised
141 as a combination of such modules when viewed down the c axis (Thompson 1978). Considering the
142 structural symmetry comprising c -glide planes that pass through individual silicate chains, such blocks

143 are only one-half unit cell wide along the b axis, and therefore a mirrored \mathbf{p} module was introduced as
144 the \mathbf{q} module (Bozhilov 2013 and references therein). This can be used to formalise generic pyribole
145 sequences for single chain sequences as $\mathbf{p}2\mathbf{M}_{(n-1)}\mathbf{q}$, and for mixed chain sequences as $\mathbf{pM}_n\mathbf{qM}_{(n-1)}$, where
146 n is a positive integer. Representation of such sequences for ferro-tschermakite and clinojimthompsonite
147 are shown on Figure 1.

148 Many TEM studies have addressed classic and NCP pyribole intergrowths as potentially metastable
149 polysomes that are intrinsic to growth processes in which kinetic steps are preserved within their fine
150 microstructures. Veblen and Buseck (1980) postulated that most common defects are the terminations of
151 (010) slabs, so called ‘zippers’. They further stipulated that coherent terminations must obey two rules:
152 (1) the chain sequences on both sides of that termination must have either an even or odd number of
153 chains; and (2) the number of sub-chains must be equal on both sides of the zipper termination, lest planar
154 faults with displacements occur at slab terminations. Reaction schemes and kinetic models were
155 developed for constraining chain width distributions in biopyribole based on such transformation rules
156 corroborated with observations of zipper terminations (e.g., Grobéty 1997).

157 The biopyribole microstructures could thus be used to interpret physicochemical processes recorded
158 during overprinting events in terranes with protracted geological histories (see reviews by Champness
159 2002 and Bozhilov 2013).

160 **METHODOLOGY**

161 Two S/TEM-foils were extracted from one magnetite grain using established dual-beam FIB-SEM
162 methods with a FEI Helios Nanolab 600 instrument (see Ciobanu et al. 2011). High Angle Annular Dark
163 Field (HAADF) STEM imaging and energy-dispersive X-ray spectrometry (EDX) spot analysis/mapping
164 of the foils were conducted with an ultra-high resolution, probe-corrected FEI Titan Themis S/TEM
165 instrument operated at 200 kV. Simultaneously Bright Field (BF) and HAADF STEM imaging was also
166 undertaken during the experimental sessions. This is equipped with a X-FEG Schottky source and Super-

167 X EDX geometry. The Super-X EDX detector provides geometrically symmetric EDX detection with an
168 effective solid angle of 0.8 Sr. Probe correction delivered sub-Ångstrom spatial resolution and an inner
169 collection angle greater than 50 mrad was used for HAADF imaging with a Fischione detector. Indexing
170 of diffraction patterns was conducted with WinWulff© (v1.6) and publicly available data from the
171 American Mineralogist Crystal Structure Database (<http://rruff.geo.arizona.edu/AMS/amcsd.php>).
172 Crystal structure models were generated in CrystalMaker® (v10.4.6) and STEM for xHREM™ (v4.1).
173 Magnetite composition along transects close to the FIB-cut samples was obtained using electron probe
174 microanalysis (EPMA) using a CAMECA SX-Five electron probe microanalyzer. Analytical procedures
175 are given in Supplemental¹ Table A1. All instruments are housed at Adelaide Microscopy, The
176 University of Adelaide.

177

RESULTS

178 The studied magnetite derives from a cm-wide band intersecting the contact between altered
179 Donington granite and a mafic dyke (?) at a depth of ~1,891 m RL (drillhole WRD33, sample
180 WW33.12B; Fig. 2a, b). Fine-grained sulfides (pyrite+chalcopyrite) form trails crosscutting the
181 magnetite band. Alteration comprises chlorite with various Fe/Mg ratios and K-feldspar/sericite.
182 Magnetite displays zonation patterns with respect to dusty, Si-bearing inclusions, and is marginally
183 replaced by hematite and infilled by sulfides and secondary chlorite+quartz, as seen along the distinct
184 zone boundaries in the analyzed grain. The STEM study was carried out on two foils, extracted from: (i)
185 across a sharp boundary -foil #1; and densely-mottled inclusion core-foil #2 (Fig. 2c, d). The two
186 locations were selected so as to probe the changes across the magnetite grain, from primary zoning (foil
187 # 1) to overprint within the core (foil # 2).

¹ Deposit item

188 EPMA data for magnetite (Supplemental¹ Table A1) shows up to 4.39 wt.% SiO₂, 2.33 wt.% Al₂O₃,
189 and measurable concentrations of MgO, CaO, TiO₂ and V₂O₃ (<1 wt.% each), elements that, with the
190 exception of SiO₂, are all common to spinel group minerals. Calculation of magnetite composition in
191 a.p.f.u. terms on a 32 O atom basis shows no significant difference between the two transects placed
192 across zone boundaries with the highest contrast in inclusion density, representing the same domains
193 sampled for the nanoscale study (Fig. 2d). Three possible types of magnetite substitution with respect to
194 Si vs. Fe exchange are shown in Figure 2e:

195 (1) $2\text{Fe}^{2+} \Leftrightarrow \text{Si}^{4+} + \text{Fe}^{2+}$, leading to $\text{Fe}^{2+}_{16}\text{Si}_8\text{O}_{32}$ (fayalite);

196 (2) $4\text{Fe}^{3+} \Leftrightarrow 3\text{Si}^{4+} + \square$, leading to $\square_4\text{Fe}^{2+}_8\text{Si}_{12}\text{O}_{32}$ (\square = vacancy);

197 (3) $\text{Fe}^{2+} + 2\text{Fe}^{3+} \Leftrightarrow 2\text{Si}^{4+} + \square$, leading to $\gamma\text{-}\square_4\text{Fe}^{2+}_4\text{Fe}^{3+}_8\text{Si}_8\text{O}_{32}$.

198 Substitution (1) preserves metal saturation, whereas the other two types require metal vacancies thus
199 leading to vacancy-bearing spinel phases such as maghemite or $\gamma\text{-Fe}_2\text{O}_3$: $(\square_{0.33}\text{Fe}^{3+}_{0.67})\text{Fe}^{3+}_2\text{O}_4$ or
200 $(\square_{2.64}\text{Fe}^{3+}_{5.36})\text{Fe}^{3+}_{16}\text{O}_{32}$ (Bosi et al. 2019). Substitution (3), was considered by Xu et al. (2014) to define
201 the formation of $\gamma\text{-}\square_{0.5}\text{Fe}_{1.5}\text{SiO}_4$ nanoprecipitates (space group *P4₃32*), one of the Si-Fe-bearing phases
202 typifying silician magnetite with ordered metal vacancies. In this case, Si replaces Fe³⁺ in tetrahedral
203 sites and vacancies are introduced in the octahedral Fe²⁺ sites of the magnetite structure.

204 When considering the ΣMe^{4+} (Si+Ti±U) vs. ΣFe diagram, the data plots close to the substitution line
205 defining the $\gamma\text{-}\square_{0.5}\text{Fe}_{1.5}\text{SiO}_4$ phase (Fig. 2f). The offset is due to the presence of other silicate inclusions
206 but the linear trend nonetheless suggests that inclusion nucleation is preferentially controlled by the
207 magnetite structure.

208 HAADF STEM imaging of the two foils shows zonation with respect to inclusions in foil #1, but
209 pervasively distributed inclusions in foil #2 (Fig. 3). In both foils, there are also coarser inclusions/clots,
210 which are identified from STEM EDX spectra and element maps as plagioclase, rutile, chlorite and
211 sericite (Supplemental¹ Figs. A1-3). Primary zonation (foil # 1) shows the sharp contact between

212 inclusion-free and -mottled bands in magnetite (Fig. 3a). A change in inclusion orientation occurs over
213 an interval of ~ 15 μm from this boundary to the other end of the foil. The junction to the last zone is
214 marked by larger mineral clots comprising phases that are not present throughout the mottling in
215 magnetite (e.g., plagioclase, rutile and fluorite; Fig. 3a; Supplemental¹ Fig. A2). The largest clot, several
216 μm in width, is present in the sample obtained from the core (foil #2; Fig. 3b). The core overprint is
217 highlighted by presence of sericite+chlorite+quartz whereas nm-scale rutile and plagioclase inclusions
218 are also present within discrete fields (Supplemental¹ Figs. A2, A3). There is also a subtle change in
219 inclusion orientation along the length of the foil.

220 Stubby grains of Al-rich amphibole, each up to several hundred nm in length and tens of nm wide
221 (Fig. 4a-c) are present at the contact to the inclusion-free zone in magnetite (Fig. 3a). On HAADF STEM
222 images, stacking disorder in the amphibole is observed as darker, single or double strips that extend along
223 the entire length of each grain but with irregular distribution across their width (Fig. 4d-f). A second
224 population of larger inclusions, consisting of chlorite+quartz, occurs in the same area with the amphibole
225 grains (Fig. 4g-i). Some longer strips of chlorite contain relicts of amphibole (Fig. 5a).

226 The host magnetite is typified by dense mottling with respect to Si-Fe-nanorods, each a few nm in
227 width, positioned along $\langle 111 \rangle_{\text{magnetite}}$ (Fig. 5a, b). Fast Fourier transform (FFT) patterns obtained from
228 amphibole tilted on the $[001]$ zone axis shows streaks along b^* indicating disorder due to the presence
229 of the darker strips stacked along this direction (Fig. 5c, d). At the same tilt, host magnetite is oriented
230 on $[11\bar{2}]$ zone axis (Fig. 5c). High resolution images show epitaxial relationships between the two
231 minerals, whereby $a_{\text{amphibole}}$ is parallel to $\langle 111 \rangle_{\text{magnetite}}$ along their mutual contact (Fig. 5e). Away from
232 the boundary between the zones of clean and inclusion-rich magnetite, longer Si-Fe-nanorods are the
233 only major inclusions observed (Fig. 6a, b). EDX mapping of areas from both foils show that the Si-Fe
234 bearing precipitates can also contain minor, albeit variable, Al-Mg-Ca content (Supplemental¹ Fig. A2).

235 An integrated STEM EDX spectra across one of the mapped amphibole grains gives the mean formula
236 ${}^A(\text{K}_{0.06}\text{Na}_{0.01})_{0.07}{}^B(\text{Ca}_{1.65}\text{Na}_{0.35})_2{}^C(\text{Fe}^{2+}_{2.07}\text{Al}_{1.64}\text{Mg}_{1.15}\text{Ti}_{0.06}\text{Fe}^{3+}_{0.04}\text{Mn}_{0.04})_5{}^T(\text{Si}_{6.48}\text{Al}_{1.52})_8\text{O}_{22}{}^W(\text{OH})_2$,
237 corresponding to ferro-tschermakite (Fig. 6d-e; Table 1). Total a.p.f.u. Al is 3.16, comparable with the
238 3.18 total a.p.f.u. Al in ferro-tschermakite reported from Ploumanac'h (Oberti et al. 2018), both slightly
239 lower than the 3.3 total a.p.f.u. Al in ferro-tschermakite reported by Hawthorne and Grundy (1973). The
240 composition of the Wirrda Well amphibole is within the limits of the tschermakite field as defined by
241 Hawthorne et al. (2012), i.e., ${}^A(\text{K}+\text{Na}) = 0.07$ a.p.f.u. (no Ca present in this site) and ${}^C(\text{Al}+\text{Fe}^{3+}+2\text{Ti})=1.8$
242 a.p.f.u.

243 High resolution imaging of (i) the amphibole and (ii) stacking defects as double-rows of a 3-chain
244 silicate shows a good match with HAADF STEM simulations and crystal structure models for (i) ferro-
245 tschermakite (Ftsk) and (ii) clinojimthompsonite (Cjt) obtained for [001] zone axis in both species (Fig.
246 7). This allows interpretation of the images in terms of atom distributions and crystal structural motifs.

247 Most prominent on the images and simulations are the arrays of 7 and 10 bright dots (Fig. 7a, b), for
248 Ftsk and Cjt, respectively. These correspond, on the crystal structure models, to the octahedron strips
249 (with the same number of atoms as dots on the images) in the middle part of each unit cell (Fig. 7c, d).
250 The pairs of SiO₄ tetrahedra (*T*) are recognized as the second brightest dots on the images and simulations
251 and correspond to the topology of the 2- and 3-pairs of *T* placed on both sides of the octahedron strips in
252 Ftsk and Cjt, respectively. In the case of Ftsk, the atoms in the *B* position, at the edges of the octahedron
253 strips, are slightly less bright than the rest of the strip with an excellent match between the image and
254 simulation using the crystal structure of Hawthorne and Grundy (1973) for Ftsk (Fig. 7a, c). The match
255 between the images and simulations for the atoms along the octahedron strip is not as good in terms of
256 relative HAADF signal intensity. Considering that the structure used for Cjt is a Mg-rich specimen
257 (Veblen and Burnham 1978), we can assume a higher proportion of heavier atoms occupying the
258 octahedron strip, e.g., higher Fe, Ca and less Mg, in the Wirrda Well sample (Fig. 7b, d).

259 The third prominent feature on the images and simulations obtained for the amphibole are the dark,
260 ‘diamond-shaped’ motifs separating the octahedron strips (Fig. 7a, c, e). These correspond to the *A*
261 cavities which host alkaline atoms \pm vacancies on the crystal structure model (Fig. 7g). Double-diamond
262 shaped motifs, with the same geometry as in the amphibole, are present on the images and simulations
263 obtained for Cjt (Fig. 7b, d, f). This implies that such *A*-type cavities should be also present in the Cjt, as
264 marked on the simulation and crystal structure model in Figure 7f, h.

265 The STEM simulations show that the atoms at the edges of the octahedron strips (*B* site) form a zig-
266 zag array, ‘zipper’ terminations along the boundaries between the 2- and 3-*I beams* structures (Fig. 8a).
267 The *I-beam* stacks can be identified also on high resolution images obtained for such intergrowths,
268 whereby the octahedron strips of 7- and 10-atoms, as well as the *A* cavities are the most prominent
269 features (Fig. 8b). In detail, the relationships between the unit cells and the topology of *I-beams* for Ftsk
270 and Cjt show that insertion of single and double arrays of 3-*I beams* correspond to 1 and 1.5 units of Cjt
271 (Fig. 9).

272 In contrast, irregular swells observed along some of the (010) zippers in the amphibole show stepwise
273 terminations and changes to the structure of the triple-chain silicate (Fig. 10a, b). In detail, alternating
274 brighter and darker strips with ~ 9.2 Å spacing, correspond to the *c* parameter of phyllosilicates such as a
275 2:1 mixture of pyrophyllite (P) and talc (T) (Drits et al. 2012 (Fig. 10b). The *I-beam* model for such areas
276 shows that the (010) boundary between the amphibole and inferred phyllosilicate mixture is coherent
277 along a “normal” biopyribole structure (‘**p**’ slab; Fig. 10c) but other planar orientations entail gaps (Fig.
278 10c). Wider chlorite patches in which no relict amphibole is preserved display disordered intergrowths
279 with other phyllosilicates, likely P/T mixtures as along the zippers in the amphibole (Fig. 10d). The
280 chlorite itself also displays irregularities in layer stacking (Fig. 10e). Indexing of phyllosilicates was done
281 using models of P/T mixtures (Drits et al. 2012) and one of the *C2/m* chlorite structures (Zanazzi et al.
282 2007) projected onto the [100] zone axis (Fig. 10 f, g).

283

DISCUSSION

284 *Significance of polysomatic disorder in ferro-tschermakite*

285 The Ftsk inclusions displaying single- and double-rows of a 3-chain silicate identified as a Ca-bearing
286 variety of Cjt represents the first report of pyriboles displaying polysomatic disorder within magnetite.
287 Isolated triple- or quintuple-chains in amphiboles are a type of chain-width disorder that have been
288 debated in terms of primary growth mechanisms (Cressey et al. 1982) and replacement with rapid growth
289 kinetics (Veblen 1981). The presence of isolated triple-chains showing no displacive planar defects at
290 the terminations of the (010) slabs in host amphibole from Wirrda Well (Figs. 4d, 5d) breaks the
291 termination rules of Veblen and Buseck (1980). In addition, the *I-beam* intergrowths, documented from
292 [001] HAADF STEM imaging, which extend along the entire length of the Ftsk inclusions, without
293 reaction fronts at mutual contacts between 3-chain zippers and host amphibole (Figs. 4, 5 and 9), are
294 suggestive of primary co-crystallisation rather than replacement. Similar conclusions were drawn for
295 Mg-(Fe)-pyriboles (jimthompsonite, chesterite and anthophyllite) and their mutual intergrowths in
296 Archean ultramafic rocks from the Isua Supracrustal Belt, West Greenland (Konishi et al. 2010).

297 In contrast, the presence of swells along the zippers (Fig. 10) supports the idea of hydration of
298 amphibole inclusions leading to their advanced pseudomorphic replacement by phyllosilicates (chlorite,
299 pyrophyllite, talc; Fig. 4) in the Wirrda Well specimen. The presence of gaps along non-coherent
300 boundaries between talc/pyrophyllite and amphibole (Fig. 10c) entail channels running parallel to the *c*
301 axis in pyribole. Such channels provide microstructures for fluid infiltration resulting in pyribole
302 hydration reactions, as first discussed for biopyriboles in the metamorphosed ultramafic body at Chester,
303 Vermont (Veblen and Buseck 1980). A wide range of microstructures have been reported and are intrinsic
304 to most polysomatic biopyribole sequences (see Bozhilov 2013 and references therein).

305 Documented occurrences from much larger, micron- to mm-scale pyribole sequences elsewhere
306 featuring polysomatic disorder include a dozen or so Mg-Fe-pyribole associations from ophiolites,

307 metamorphosed ultramafic complexes or other metamorphic terranes, as well as an extra-terrestrial
308 carbonaceous chondrite (see Bozhilov 2013). None of the reported occurrences include an Al-rich, calcic
309 amphibole, as shown here for Wirrda Well.

310 Chain-width disorder was, however, encountered as triple and quadruple chains in synthetic Al-rich
311 amphibole with $X_{\text{Tsk}}=0.13$ (X =mol.% tschermakite; 2.83 wt.% Al_2O_3) from the tremolite-tschermakite
312 solid solution (Najorka and Gottschalk 2003). These amphiboles were synthesized at 750 °C and 500
313 MPa in 30-day runs, whereas defect-free structures with $X_{\text{Tsk}}=0.39$ (8 wt.% Al_2O_3) were obtained using
314 shorter (5-day) runs at slightly higher T (800 °C) and far higher P (1,500 MPa) (Najorka and Gottschalk
315 2003). The formation conditions of triple-chain silicates were also assessed experimentally and
316 thermochemically showing that Na-Cjt is stable at metamorphic conditions of 2 kbar and 450 °C, or could
317 form by reactions between igneous minerals (enstatite, forsterite) in oceanic harzburgite and seawater at
318 temperatures up to 300 °C (Ams and Jenkins 2011). Na-free Cjt is estimated to be stable at comparable
319 conditions to Na-Cjt, with both NCP being postulated to occur in oceanic hydrothermal environments
320 and geothermal systems but not in serpentinized ultramafic rocks (Ams and Jenkins 2011).

321 *Genetic considerations*

322 Irrespective of the chain-width disorder, experimental runs showing a positive correlation between Al
323 content in amphibole and total pressure (e.g., Najorka and Gottschalk 2003) support the trend recognized
324 empirically from many petrological studies of igneous and metamorphic rocks. Hammarstrom and Zen
325 (1986) introduced the Al-in-hornblende geobarometer based on the dependence of the total Al content
326 (Al^{tot} a.p.f.u.) of igneous hornblende on pressure via the so-called “Tschermak exchange reactions” in
327 low variance granitoid systems at near solidus conditions. We can assume that Ftsk and plagioclase,
328 found within a few nm up to several μm from one another (Fig. 3a), are buffered by host magnetite and
329 thus the assemblage fulfils the textural equilibration criteria required for application of the barometer.
330 High pressure estimates (~11.5 kbar) are obtained for the Wirrda Well assemblage hosted in Donington

331 granite, giving a Al^{tot} value of 3.16 in ferro-tschermakite and using the formula P (kbar) = $0.5 + 0.331(8)$
332 $\times Al^{tot} + 0.995(4) \times (Al^{tot})^2$ for the revised Al-in-hornblende geobarometer (Mutch et al. 2016). Although
333 this revised geobarometer targeted low-pressure granitoids, amphibole compositions from earlier
334 experimental calibrations at pressures as high as 15 kbar (Schmidt 1992) were included in the Al^{tot} vs.
335 pressure plot (Fig. 10c in Mutch et al. 2016). Wirrda Well Ftsk lies within the range of synthetic
336 amphiboles with Al^{tot} of 3.042 and 3.349 a.p.f.u obtained at 11.5 and 13 kbar, respectively (Schmidt
337 1992).

338 Nevertheless, the silician magnetite with Ftsk inclusions most likely formed after intrusion
339 emplacement since the igneous accessory magnetite is Si-free (and associated with ilmenite), whereas
340 the amphibole is pargasitic in fresh Donington granite elsewhere in the Gawler Craton (Keyser et al.
341 2019). Of the two major geological events that affected the region after ~ 1.85 Ga (emplacement of
342 Donington granite and coeval dolerite dikes), the 1735–1690 Ma regional metamorphism is likely
343 responsible for formation of magnetite accumulations along granite-dyke contacts.

344 Regional metamorphism at amphibolite facies is supported not only by the pressure estimate of ~ 11.5
345 kbar from amphibole geobarometry but also by the observed assemblages which include plagioclase, the
346 latter forming as mineral clots at junctions between zones in magnetite with inclusions of different
347 orientation (Fig. 3a). Such intra-grain textures are also representative of syn-metamorphic mineral
348 growth under oriented stress. Thus, we consider magnetite accumulation via metamorphic segregation,
349 whereby impurities of Si, Al, Mg, Ca, etc., were likely provided by alteration of pre-existing lithologies,
350 particularly at granite-dolerite contacts (Fig. 2). Formation of Si-Fe-nanorods in magnetite promotes
351 preferential amphibole growth along these structures as the prograde metamorphism reaches its peak.
352 This interpretation is also supported by the linear trend observed on the ΣMe^{4+} vs. ΣFe plot for silician
353 magnetite (Fig. 2f). In detail, epitaxial growth of amphibole in magnetite can be explained by considering
354 the role of Si-rich $\langle 111 \rangle$ platelets acting as nucleation points. Cation diffusion is easily promoted within

355 the framework of oxygen packing along $\langle 111 \rangle$ directions in spinel group minerals, and matching (100)
356 planes of distorted oxygen arrays in inosilicates.

357 Retrograde reactions such as replacement of amphibole inclusions by chlorite/phyllsilicate (Fig. 10)
358 are associated with fractures affecting magnetite grain cores (Fig. 2c, d) and obliterating the amphibole
359 inclusions in foil # 2 (Fig. 3). Such an overprint is recorded at Wirrda Well by U-bearing hematite that
360 formed during the ~ 1.6 Ga IOCG event (Courtney-Davies et al. 2019). The host lithologies are largely
361 impacted by chloritization/sericitization that obliterates prograde metamorphic associations like those
362 preserved in silician magnetite.

363 The Wirrda Well silician magnetite differs from that observed at Olympic Dam in terms of the type
364 of silicate inclusions. Inclusion species also include calcic amphiboles and Al-rich silicates but these are
365 represented at Olympic Dam by (ferro)actinolite and (clino)zoisite rather than Ftsk (Ciobanu et al.
366 2019b). Such calc-silicate association was attributed to alkali-calcic alteration of the ~ 1.6 Ga Roxby
367 Downs granite, host to the Olympic Dam deposit (Ciobanu et al. 2019b; Verdugo-Ihl et al. 2020a).
368 Moreover, epidote is also present in early alteration of feldspars at Olympic Dam (Kontonikas-Charos et
369 al. 2018).

370 **IMPLICATIONS**

371 Although mineral association(s) can strongly impact the Al content in amphibole, as shown by
372 presence of high-Al hornblende (up to 3.3 a.p.f.u. Al) in low-pressure metacarbonates (Léger and Ferry
373 1991), P-T-X phase equilibria used for modelling such assemblages do not include magnetite. The role
374 played by magnetite in buffering reactions among biopyriboles or their polysomatic disorder has not yet
375 been tested experimentally. One example analogous to the case study here is the coherent nanoscale
376 intergrowths between spinel group minerals and aluminous, Ca-amphibole that are reported as lamellar
377 exsolutions in chromite from high-pressure terranes such as podiform chromitite from the Nakhil Massif,
378 Semail Ophiolite, Oman (Chen et al. 2019).

379 Unlike hematite, which is typified by a common U-W-Sn-Mo signature throughout the lifespan of
380 IOCG mineralizing systems in the Olympic Dam district (Verdugo-Ihl et al. 2017, 2019, 2020b;
381 Courtney-Davies et al. 2019, 2020a), magnetite records distinct geochemical/nano-inclusion signatures
382 dependent on the local geological setting. For example, at Acropolis, a prospect ~17 km west of Wirrda
383 Well that is hosted by volcanic sequences, magnetite is Ti-rich and typified by inclusions of spinel
384 (Verdugo-Ihl et al. 2021) analogous to those in igneous granite-hosted magnetite from Olympic Dam
385 (Ciobanu et al. 2019b; Verdugo-Ihl et al. 2020a). Uranium-Pb dating of silician magnetite from Olympic
386 Dam shows the likely presence of older Fe-rich protoliths and ~1760 Ma granitoids (Courtney-Davies et
387 al. 2020b). Elsewhere, actinolite is recognized among the otherwise wide range of nanomineral
388 inclusions in Fe-oxides from the Los Colorados IOCG deposit, Chilean Iron Belt (Deditius et al. 2018).

389 Proof of concept for the use of nanoscale Ftsk inclusions in magnetite as a mineral geobarometer is
390 seen in the reliable application of ilmenite-magnetite nano-thermobarometry with estimated T - fO_2
391 values from compositions of mineral pairs measured at the nanoscale (Righter et al. 2014; Verdugo-Ihl
392 et al. 2021). The assemblage described here from Wirrda Well represents a ~1735–1690 Ma metamorphic
393 window preserved in magnetite that was inherited from ~1.85 Ga lithologies, and with a subsequent
394 IOCG-fluid overprint at ~1.6 Ga. Nanoscale studies of magnetite, if considered in an appropriate
395 petrological context, can provide valuable insights into the evolution of mineralizing systems within the
396 same district and, as more studies become available, also across distinct metallogenic provinces
397 worldwide. Likewise, confirmation of nanomineral Ftsk pressure estimates by petrological studies show
398 the potential value of magnetite in recording and preserving evidence for discrete events in terranes with
399 protracted geological histories.

400 HAADF STEM imaging gives an improved visualization of pyribole structures and particularly the
401 distribution and topology of *A* cavities (Figs. 7-9), which are the sites with the greatest probability of
402 containing heterovalent SRO (Hawthorne et al. 2005). This type of imaging should provide further

403 insight into polysomes such as those between (cavity free) pyroxenes and amphiboles, as for example
404 the sequence ‘2111’ reported from anthophyllite in ultramafic lenses (Leontine Alps, Switzerland;
405 Grobety 1996) and subsequently the subject of debate as to whether these are artifacts or natural products
406 (Konishi et al. 2004).

407 The occurrence of chain-width disorder during pyribole crystallization is most likely the rule rather
408 than the exception in minerals that share crystal structural blocks. Recent HAADF STEM studies have
409 also revealed intergrowths of single units or individual sub-structural motifs relating to stacking disorder
410 recorded during crystallisation among members of diverse modular homologous series, e.g., REE-
411 fluorocarbonates (Ciobanu et al. 2017), mixed-layer chalcogenides (Cook et al. 2019), or Sb-Bi-sulfosalts
412 with chessboard structures (Li et al. 2019).

413 **ACKNOWLEDGEMENTS**

414 This is a contribution to the ‘FOX’ project (Trace elements in iron oxides: deportment, distribution and
415 application in ore genesis, geochronology, exploration and mineral processing), supported by BHP Olympic Dam
416 and the South Australian Government Mining and Petroleum Services Centre of Excellence. We acknowledge
417 reviews by Fernando Cámara, David M. Jenkins, and an anonymous reviewer, and manuscript handling by
418 Associate Editor Simon Redfern.

419 **REFERENCES CITED**

- 420 Abdu, Y.A., and Hawthorne, F.C. (2009) Crystal structure and Mössbauer spectroscopy of tschermakite from the
421 Ruby locality at Fiskenaasset, Greenland. *The Canadian Mineralogist*, 47, 917–926.
422 <https://doi.org/10.3749/canmin.47.4.917>
- 423 Ams, B.E., and Jenkins, D.M. (2011) Formation conditions for triple-chain silicates. *American Mineralogist*, 96,
424 814–819. <https://doi.org/10.2138/am.2011.3568>
- 425 Bosi, F., Biagioni, C., and Pasero, M. (2019) Nomenclature and classification of the spinel supergroup. *European*
426 *Journal of Mineralogy*, 31, 183–192.

- 427 Bozhilov, K.N. (2013) Structures and microstructures of non-classical pyriboles. *EMU Notes in Mineralogy*, 14,
428 109–152.
- 429 Champness, P.E. (2002) Applications of Transmission Electron Microscopy. In: *Advances in Imaging and*
430 *Electron Physics*, vol. 121, p. 53–90, Academic Press. [https://doi.org/10.1016/S1076-5670\(02\)80025-8](https://doi.org/10.1016/S1076-5670(02)80025-8)
- 431 Chen, T., Jin, Z., Zhang, J., and Wang, L. (2019) Calcium amphibole exsolution lamellae in chromite from the
432 Semail ophiolite: Evidence for a high-pressure origin. *Lithos*, 334–335, 273–280.
433 <https://doi.org/10.1016/j.lithos.2019.03.020>
- 434 Ciobanu, C.L., Cook, N.J., Utsunomiya, S., Pring, A., and Green, L. (2011) Focussed ion beam–transmission
435 electron microscopy applications in ore mineralogy: Bridging micro- and nanoscale observations. *Ore Geology*
436 *Reviews*, 42, 6–31. <https://doi.org/10.1016/j.oregeorev.2011.06.012>
- 437 Ciobanu, C.L., Cook, N.J., Maunders, C., Wade, B.P., and Ehrig, K. (2016) Focused Ion Beam and Advanced
438 Electron Microscopy for Minerals: Insights and Outlook from Bismuth Sulphosalts. *Minerals*, 6, 112.
439 <https://doi.org/10.3390/min6040112>
- 440 Ciobanu, C.L., Kontonikas-Charos, A., Slattery, A., Cook, N.J., Ehrig, K., and Wade, B.P. (2017) Short-range
441 stacking disorder in mixed-layer compounds: a HAADF STEM study of bastnäsite-parisite intergrowths.
442 *Minerals*, 7, 227. <https://doi.org/10.3390/min7110227>
- 443 Ciobanu, C.L., Utsunomiya, S., Reich, M., Plümper, O., and Cook, N.J. (2019a) Editorial for Special Issue
444 “Minerals Down to the Nanoscale: A Glimpse at Ore-Forming Processes”. *Minerals*, 9, 692.
445 <https://doi.org/10.3390/min9110692>
- 446 Ciobanu, C.L., Verdugo-Ihl, M.R., Slattery, A., Cook, N.J., Ehrig, K., Courtney-Davies, L., and Wade, B.P.
447 (2019b) Silician Magnetite: Si–Fe-Nanoprecipitates and Other Mineral Inclusions in Magnetite from the
448 Olympic Dam Deposit, South Australia. *Minerals*, 9, 311. <https://doi.org/10.3390/min9050311>
- 449 Cook, N.J., Ciobanu, C.L., Liu, W.Y., Slattery, A., Wade, B.P., Mills, S., and Stanley, C.J. (2019) Polytypism and
450 polysomatism in mixed-layer chalcogenides: characterization of $\text{PbBi}_4\text{Te}_4\text{S}_3$ and inferences for ordered phases
451 in the aleksite series. *Minerals*, 9, 628. <https://doi.org/10.3390/min9100628>
- 452 Courtney-Davies, L., Ciobanu, C.L., Verdugo-Ihl, M.R., Dmitrijeva, M., Cook, N.J., Ehrig, K., and Wade, B.P.
453 (2019) Hematite geochemistry and geochronology resolve genetic and temporal links among iron-oxide copper

- 454 gold systems, Olympic Dam district, South Australia. *Precambrian Research* 335, 105480.
455 <https://doi.org/10.1016/j.precamres.2019.105480>
- 456 Courtney-Davies, L., Ciobanu, C.L., Tapster, S.R., Cook, N.J., Ehrig, K., Crowley, J.L., Verdugo-Ihl, M.R., Wade,
457 B.P., and Condon, D.J. (2020a) Opening the Magmatic-Hydrothermal Window: High-Precision U-Pb
458 Geochronology of the Mesoproterozoic Olympic Dam Cu-U-Au-Ag Deposit, South Australia. *Economic*
459 *Geology*, 115, 1855-1870, <https://doi.org/10.5382/econgeo.4772>.
- 460 Courtney-Davies, L., Ciobanu, C.L., Verdugo-Ihl, M.R., Cook, N.J., Ehrig, K., Wade, B.P., Zhu, Z.-Y., and
461 Kamenetsky, V.S. (2020b) ~1760 Ma magnetite-bearing protoliths in the Olympic Dam deposit, South
462 Australia: Implications for ore genesis and regional metallogeny. *Ore Geology Reviews*, 118, 103337.
463 <https://doi.org/10.1016/j.oregeorev.2020.103337>
- 464 Cressey, B.A., Whittaker, E.J.W., and Hutchison, J.L. (1982) Morphology and alteration of asbestiform grunerite
465 and anthophyllite. *Mineralogical Magazine*, 46, 77–87.
- 466 Deditius, A.P., Reich, M., Simon, A.C., Suvorova, A., Knipping, J., Roberts, M.P., Rubanov, S., Dodd, A., and
467 Saunders, M. (2018) Nanogeochemistry of hydrothermal magnetite. *Contributions to Mineralogy and*
468 *Petrology*, 173, 46. <https://doi.org/10.1007/s00410-018-1474-1>
- 469 Deer, W.A., Howie, R.A., and Zussman, J. (2013) *An Introduction to the Rock-Forming Minerals*, 3rd edition.
470 Mineralogical Society of Great Britain and Ireland, <https://doi.org/10.1180/DHZ>.
- 471 Drits, V.A., Guggenheim, S., Zviagina, B.B., and Kogure, T. (2012) Structures of the 2:1 layers of pyrophyllite
472 and talc. *Clays and Clay Minerals*, 60, 574-587. <https://doi.org/10.1346/CCMN.2012.0600603>
- 473 Fleet, M.E., Bilcox, G.A., and Barnett, R.L. (1980) Oriented magnetite inclusions in pyroxenes from the Grenville
474 Province. *Canadian Mineralogist*, 18, 89–99.
- 475 Gao, W., Ciobanu, C.L., Cook, N.J., Slattery, A., Huang, F., and Wang, D. (2019a) Nanoscale study of lamellar
476 exsolutions in clinopyroxene from olivine gabbro: Recording crystallization sequences in iron-rich layered
477 intrusions. *American Mineralogist*, 104, 244–261. <https://doi.org/10.2138/am-2019-6764>
- 478 Gao, W., Ciobanu, C.L., Cook, N.J., Slattery, A., Huang, F., and Song, D. (2019b) Nanoscale study of
479 titanomagnetite from the Panzhihua Layered Intrusion, Southwest China: Multistage exsolutions record ore
480 formation. *Minerals*, 9, 513. <https://doi.org/10.3390/min9090513>

- 481 Grobety, B.H. (1996) New short-range biopyribole polysomes from the Lepontine Alps, Switzerland. American
482 Mineralogist, 81, 404–417. <https://doi.org/10.2138/am-1996-3-415>
- 483 Grobety, B.H. (1997) The replacement of anthophyllite by jimthompsonite: a model for hydration reactions in
484 biopyriboles. Contributions to Mineralogy and Petrology, 127, 237-247.
- 485 Hammarstrom, J.M., and Zen, E-an (1986) Aluminum in hornblende: An empirical igneous geobarometer.
486 American Mineralogist, 71, 1297–1313.
- 487 Hawthorne, F., and Grundy, H. (1973) The crystal chemistry of the amphiboles. I: Refinement of the Crystal
488 structure of ferrotschermakite. Mineralogical Magazine, 39, 36-48.
- 489 Hawthorne, F.C., Della Ventura, G., Oberti, R., Robert, J.-L., and Iezzi, G. (2005) Short-range order in minerals:
490 Amphiboles. The Canadian Mineralogist, 43, 1895–1920. <https://doi.org/10.2113/gscanmin.43.6.1895>
- 491 Hawthorne, F.C., Oberti, R., Harlow, G.E., Maresch, W.V., Martin, R.F., Schumacher, J.C., and Welch, M.D.
492 (2012) Nomenclature of the amphibole supergroup. American Mineralogist, 97, 2031–2048.
493 <https://doi.org/10.2138/am.2012.4276>
- 494 Keyser, W., Ciobanu, C.L., Cook, N.J., Courtney-Davies, L., Kennedy, A., Wade, B.P., Ehrig, K., Dmitrijeva, M.,
495 Kontonikas-Charos, A., Feltus, H., and Johnson, G. (2019) Petrographic and geochronological constraints on
496 the granitic basement to the Middleback Ranges, South Australia. Precambrian Research, 324, 170-193.
497 <https://doi.org/10.1016/j.precamres.2019.01.024>
- 498 Konishi, H., Akai, J., Kurokawa, K. (1993) Calcic analog of clinojimthompsonite from the Oeyama ophiolite,
499 southwest Japan. Journal Geological Society Japan, 99, 679-682
- 500 Konishi, H., Alviola, R., and Buseck, P.R. (2004) 2111 biopyribole intermediate between pyroxene and amphibole:
501 Artifact or natural product? American Mineralogist, 89, 15-19. <https://doi.org/10.2138/am-2004-0103>
- 502 Konishi, H., Xu, H., and Dymek, R.F. (2010) High-resolution TEM study of jimthompsonite, chesterite, and chain-
503 width disorder in Archean ultramafic rocks from Isua, West Greenland. American Mineralogist, 95, 73–80.
504 <https://doi.org/10.2138/am.2010.3212>
- 505 Kontonikas-Charos, A., Ciobanu, C.L., Cook, N.J., Ehrig, K., Ismail, R., Krneta, S., and Basak, A. (2018) Feldspar
506 mineralogy and rare earth element (re)mobilization in iron-oxide copper gold systems from South Australia: a
507 nanoscale study. Mineralogical Magazine, 82(S1), S173–S197. <https://doi.org/10.1180/minmag.2017.081.040>

- 508 Léger, A., and Ferry, J.M. (1991) Highly aluminous hornblende from low-pressure metacarbonates and a
509 preliminary thermodynamic model for the Al content of calcic amphibole. *American Mineralogist*, 76, 1002–
510 1017.
- 511 Li, W., Ciobanu, C.L., Slattery, A., Cook, N.J., Liu, W., Wade, B.P., and Xie, G.Q. (2019) Chessboard structures:
512 atom-scale imaging of homologues from the kobellite series. *American Mineralogist*, 104, 459–462.
- 513 Locock, A.J. (2014) An Excel spreadsheet to classify chemical analyses of amphiboles following the IMA2012
514 recommendations. *Computers & Geosciences*, 62, 1–11.
- 515 Medlin, D.L., Ramasse, Q.M., Spataru, C.D., and Yang, N.Y.C. (2010) Structure of the (0001) basal twin boundary
516 in Bi₂Te₃. *Journal of Applied Physics*, 108, 043517. <https://doi.org/10.1063/1.3457902>
- 517 Medlin, D.L., and Snyder, G.J. (2013) Atomic-scale interfacial structure in rock salt and tetradymite chalcogenide
518 thermoelectric materials. *JOM*, 65, 390–400. <https://doi.org/10.1007/s11837-012-0530-y>
- 519 Medlin, D., Erickson, K., Limmer, S., Yelton, W., and Siegal, M.P. (2014) Dissociated 1/3 <0111> dislocations
520 in Bi₂Te₃ and their relationship to seven-layer Bi₃Te₄ defects. *Journal of Materials Science*, 49, 3970–3979.
- 521 Medlin, D.L., Yang, N., Spataru, C.D., Hale, L.M., and Mishin, Y. (2019) Unraveling the dislocation core structure
522 at a van der Waals gap in bismuth telluride. *Nature Communications*, 10, 1820. [https://doi.org/10.1038/s41467-](https://doi.org/10.1038/s41467-019-09815-5)
523 019-09815-5
- 524 Mutch, E.J.F., Blundy, J.D., Tattitch, B.C., Cooper, F.J., and Brooker, R.A. (2016) An experimental study of
525 amphibole stability in low-pressure granitic magmas and a revised Al-in-hornblende geobarometer.
526 *Contributions to Mineralogy and Petrology*, 171, 85. <https://doi.org/10.1007/s00410-016-1298-9>
- 527 Najorka, J., and Gottschalk, M. (2003) Crystal chemistry of tremolite–tschermakite solid solutions. *Physics and*
528 *Chemistry of Minerals*, 30, 108–124. <https://doi.org/10.1007/s00269-002-0291-1>
- 529 Oberti, R., Boiocchi, M., Hawthorne, F.C., and Ciriotti, M.E. (2018) Ferro-tschermakite from the Ploumanac’h
530 granitic complex, Brittany, France: mineral description. *European Journal of Mineralogy*, 30, 171–176.
531 <https://doi.org/10.1127/ejm/2018/0030-2700>
- 532 Papike, J.J., and Ross, M. (1970) Gedrites – crystal structures and intracrystalline cation distributions. *American*
533 *Mineralogist*, 55, 1945–1972.

- 534 Reid, A. (2019) The Olympic Cu-Au Province, Gawler Craton: A Review of the Lithospheric Architecture,
535 Geodynamic Setting, Alteration Systems, Cover Successions and Prospectivity. *Minerals*, 9, 371.
536 <https://doi.org/10.3390/min9060371>
- 537 Righter, K., Keller, L.P., Rahman, Z., and Christoffersen, R. (2014) Redox-driven exsolution of iron titanium
538 oxides in magnetite in Miller Range (MIL) 03346 nakhlite: Evidence for post crystallization oxidation in the
539 nakhlite cumulate pile? *American Mineralogist*, 99, 2313–2319. <https://doi.org/10.2138/am-2014-4926>
- 540 Schmidt, M.W. (1992) Amphibole composition in tonalite as a function of pressure: an experimental calibration
541 of the Al-in-hornblende barometer. *Contributions to Mineralogy and Petrology*, 110, 304-310.
- 542 Thompson Jr., J.B. (1978) Biopyriboles and polysomatic series. *American Mineralogist*, 63, 239–249.
- 543 Utsunomiya, S., and Ewing, R.C. (2003) Application of high-angle annular dark field scanning transmission
544 electron microscopy, scanning transmission electron microscopy-energy dispersive X-ray spectrometry, and
545 the energy-filtered transmission electron microscopy to the characterization of nanoparticles in the
546 environment. *Environmental Science and Technology*, 37, 786–791.
- 547 Van Tendeloo, G., Bals, S., Van Aert, S., Verbeeck, J., and Van Dyck, D. (2012) Advanced electron microscopy
548 for advanced materials. *Advanced Materials*, 24, 5655–5675. <https://doi.org/10.1002/adma.201202107>
- 549 Veblen, D.R. (1981) Non-classical pyriboles and polysomatic reactions in biopyriboles. In D.R. Veblen, Ed.,
550 Amphiboles and Other Hydrous Pyriboles—*Mineralogy*, 9A, p. 189–234. *Reviews in Mineralogy*,
551 Mineralogical Society of America, Chantilly, Virginia.
- 552 Veblen, D.R. (1992) Electron microscopy applied to nonstoichiometry, polysomatism, and replacement reactions
553 in minerals. *Reviews in Mineralogy and Geochemistry*, 27, 181-229.
- 554 Veblen, D.R., and Burnham, C.W. (1978) New biopyriboles from Chester, Vermont: II. The crystal chemistry of
555 jimthompsonite, clinojimthompsonite, and chesterite, and the amphibole-mica reaction. *American*
556 *Mineralogist*, 63, 1053–1073.
- 557 Veblen, D.R., and Buseck, E.R. (1979) Chain-width order and disorder in biopyriboles. *American Mineralogist*,
558 64, 687–700.
- 559 Veblen, D.R. and Buseck, P.R. (1980) Microstructures and reaction mechanisms in biopyriboles. *American*
560 *Mineralogist*, 65, 599–623.

- 561 Veblen, D.R. and Buseck, P.R. (1981) Hydrous pyriboles and sheet silicates in pyroxenes and uralites; intergrowth
562 microstructures and reaction mechanisms. *American Mineralogist*, 66, 1107–1134.
- 563 Veblen, D.R., Buseck, P.R., and Burnham, C.W. (1977) Asbestiform chain silicates: New minerals and structural
564 groups. *Science*, 198, 359–365.
- 565 Veblen, D.R., Banfield, J.F., Guthrie, G.D., Heaney, P.J., Ilton, E.S., Livi, K.J.T., and Smelik, E.A. (1993) High-
566 resolution and analytical transmission electron microscopy of mineral disorder and reactions. *Science*, 260,
567 1465-1472.
- 568 Verdugo-Ihl, M.R., Ciobanu, C.L., Cook, N.J., Ehrig, K.J., Courtney-Davies, L., and Gilbert, S. (2017) Textures
569 and U-W-Sn-Mo signatures in hematite from the Olympic Dam Cu-U-Au-Ag deposit, South Australia:
570 Defining the archetype for IOCG deposits. *Ore Geology Reviews*, 91, 173–195.
571 <https://doi.org/10.1016/j.oregeorev.2017.10.007>
- 572 Verdugo-Ihl, M.R., Ciobanu, C.L., Slattery, A., Cook, N.J., Ehrig, K., and Courtney-Davies, L. (2019). Copper-
573 arsenic nanoparticles in hematite: fingerprinting fluid-mineral interaction. *Minerals*, 9, 388.
574 <https://doi.org/10.3390/min9070388>
- 575 Verdugo-Ihl, M.R., Ciobanu, C.L., Cook, N.J., Ehrig, K.J., and Courtney-Davies, L. (2020a) Defining early stages
576 of IOCG systems: evidence from iron oxides in the outer shell of the Olympic Dam deposit, South Australia.
577 *Mineralium Deposita*, 55, 429–452. <https://doi.org/10.1007/s00126-019-00896-2>
- 578 Verdugo-Ihl, M., Ciobanu, C.L., Cook, N.J., Ehrig, K., Slattery, A., and Courtney-Davies, L. (2020b) Trace-
579 element remobilisation from W–Sn–U–Pb zoned hematite: Nanoscale insights into a mineral geochronometer
580 behaviour during interaction with fluids. *Mineralogical Magazine* 84, 502-516.
581 <https://doi.org/10.1180/mgm.2020.49>
- 582 Verdugo-Ihl, M.R., Ciobanu, C.L., Cook, N.J., Ehrig, K.J., Slattery A., Courtney-Davies, L and Dmitrijeva M.
583 (2021) Nanomineralogy of hydrothermal magnetite from Acropolis, South Australia: Genetic implications for
584 iron-oxide copper gold mineralization. *American Mineralogist*, in press, [https://doi.org/10.2138/am-2020-](https://doi.org/10.2138/am-2020-7557)
585 7557.

586 Xu, H., Shen, Z., and Konishi, H. (2014) Si-magnetite nano-precipitates in silician magnetite from banded iron
587 formation: Z-contrast imaging and ab initio study. American Mineralogist, 99, 2196–2202.
588 <https://doi.org/10.2138/am-2014-4964>

589 Yin, S., Wirth, R., Ma, C.Q., and Xu, J.N. (2019) The role of mineral nanoparticles at a fluid-magnetite interface:
590 Implications for trace-element uptake in hydrothermal systems. American Mineralogist, 104, 1180–1188.

591 Zanazzi, P.F., Montagnoli, M., Nazzareni, S., and Comodi, P. (2007) Structural effects of pressure on monoclinic
592 chlorite: A single-crystal study. American Mineralogist, 92, 655–661.

593 **FIGURE CAPTIONS**

594 **Figure 1.** (a, b) Atom filling models for crystal structures of ferro-tschemakite and clinojimthompsonite projected
595 onto [001] showing occupancy of cation sites as marked. Crystallographic information data from Hawthorne
596 and Grundy (1973) and Veblen and Burnham (1978). The two building blocks, ‘mica (M)’ and ‘pyroxene (p,
597 q)’, each of ~4.5 Å length, are also marked and separated by dashed lines. Yellow and green overlays show the
598 2- and 3-*I beam* configurations for the double and triple chain silicate, in this case, ferro-tschemakite and
599 clinojimthompsonite, respectively. Note that these can be also formalized as ‘pMqM’ and ‘pMMqMM’
600 sequences across one-unit cell whereby the *b* length corresponds to 4.5 Å x 4 (~18 Å) and 4.5 Å x 6 (~27 Å)
601 for the double and triple chain silicate, respectively.

602 **Figure 2.** (a) Photograph of drill core sample from which the studied sample was cut. Magnetite (Mt) forms a band
603 at the contact between altered granite and dolerite (?). (b, c) Reflected light images showing details of magnetite
604 grains. Note trails of sulfides crosscutting the magnetite band in (b). Crystal zoning with respect to fine, dusty
605 inclusions in magnetite can be seen in (c). Back scatter electron (BSE) image showing location of the two FIB
606 cuts from which S/TEM foils were prepared. Abbreviations: Cp=chalcopyrite; Py=pyrite. (e) Plot of Si (a.p.f.u.)
607 vs. ΣFe (a.p.f.u.) showing three types of magnetite substitution involving Si versus Fe exchange. The end-
608 member phases are marked with stoichiometry calculated on the basis of 32 oxygen atoms. Substitution (1) is
609 towards fayalite and preserves full metal occupancy, whereas the other two substitutions involve Fe vacancies
610 (□). Substitution (3) depicts cation exchange with metal vacancies in the octahedral Fe²⁺ sites coupled with Si
611 replacement of Fe³⁺ in tetrahedral sites of the magnetite structure, leading to the $\gamma\text{-}\square_4\text{Fe}^{2+}_4\text{Fe}^{3+}_8\text{Si}_8\text{O}_{32}$ (or $\gamma\text{-}$

612 $\text{Fe}_{1.5}\text{SiO}_4$) phase with $P4_332$ symmetry if vacancy ordering is encountered (Xu et al. 2014). (f) Plot ΣMe^{4+}
613 $(\text{Si}+\text{Ti}\pm\text{U}; \text{a.p.f.u.})$ vs. ΣFe (a.p.f.u.) for analyzed magnetite using stoichiometry on a 32 O atom basis
614 (Supplemental¹ Table A1). The data plot close to substitution line (3), albeit with an offset due to the presence
615 of other silicate inclusions. The linear trend suggests, nonetheless, that inclusion nucleation is preferentially
616 controlled by the magnetite structure.

617 **Figure 3.** Overview of the studied S/TEM foils, also indicating mapped areas and locations of inclusions and Si-
618 Fe-nanorods discussed in the text. Growth zones in magnetite with changes in orientation of inclusions are
619 marked by dashed lines in (a). Also note inclusion clots in both foils. Abbreviations: Chl-chlorite, Plag-
620 plagioclase, Qz-quartz, Rt-rutile, Ser-sericite, Ftsk-ferro-tschemakite.

621 **Figure 4.** Images of inclusions in magnetite from foil # 1 representing aspects as written in the headings for each
622 panel. Note high density of amphibole (circled in red) relative to chlorite (circled in yellow) as shown in (b).
623 Triple-chain silicate in amphibole marked by arrowheads on (d-f). Abbreviations: BF-Bright Field; Chl-
624 chlorite; Ftsk-ferro-tschemakite; Mt=magnetite; P=pyrophyllite; Phyl=phyllosilicate; T=talc.

625 **Figure 5.** HAADF STEM images (a, b, d, e) and Fast Fourier Transform (FFT) pattern (c) for ferro-tschemakite
626 (Ftsk) inclusions in silician magnetite. (a) Ferro-tschemakite and Si-Fe-rods oriented along $\langle 111 \rangle$ in magnetite
627 (Mt). Note chlorite (Chl) replacing the amphibole. (b) Image and FFT pattern (inset) of Si-Fe-rod in magnetite.
628 (c) FFT pattern of amphibole inclusion in magnetite showing epitaxial intergrowths between the two minerals
629 sharing orientations as marked. White and yellow rectangles correspond to ferro-tschemakite and magnetite,
630 respectively. Note strong disorder along the b^* axis in the amphibole due to the presence of triple-chain silicate
631 zippers. (d) Ferro-tschemakite grain with single rows of triple-chain silicate along the entire length of the
632 grain. (e) High resolution image of the boundary between magnetite and ferro-tschemakite inclusions showing
633 epitaxial relationships along directions as marked.

634 **Figure 6.** (a) HAADF STEM image and superimposed Si element map showing Si-Fe rods and plagioclase (Plag)
635 inclusion. (b) STEM EDX profile through magnetite and across Si-Fe rods indicated in (a). (c) HAADF STEM
636 image and STEM EDX element maps of ferro-tschemakite inclusion for selected elements. (d) Integrated
637 STEM EDX spectrum for ferro-tschemakite inclusion in (c). (e) EDX signals for Al, Ca and Mg across the
638 inclusion in (c). Abbreviations: Ftsk-ferro-tschemakite; Mt-magnetite.

639 **Figure 7.** Comparison between high resolution HAADF STEM images, simulations (shown for slice # 10 and
640 probe size 1; see Supplemental¹ Fig. A4 for additional explanation) and crystal structure models for ferro-
641 tschermakite (Ftsk) and clinojimotothompsonite (Cjt) on [001] zone axis. (a) Defect-free amphibole and (b) double
642 rows of 3-chain silicate (dashed lines) occurring in amphibole. Both images show patterns with arrays of 7-
643 and 10-brightest dots (yellow circles) flanked by 2- and 3-pairs of less bright dots (blue circles). (c) Simulation
644 of Ftsk reproduces the acquired image whereby the cations along the octahedron strip and the double-pairs of
645 Si cations (*T* sites) correspond to the yellow and blue circles in (a). Note the intensity variation along the
646 octahedron strip on the image fits perfectly the simulation, in concordance with the compositional similarity
647 between the analyzed amphibole and the Ftsk used for simulation (Hawthorne and Grundy 1973). (d)
648 Simulation of Cjt showing the 10-atoms along the octahedron strip flanked by 3-pairs of Si atoms (*T* sites),
649 topology typical of the 3-chain silicate. Note these features are readily recognizable on the image in (b).
650 However, the variation of signal intensity along the octahedron strip differs between the simulation and image,
651 indicating that the imaged 3-chain silicate differs compositionally (a Ca-, Fe-richer variety?) from the Mg-rich
652 Cjt specimen used for simulation (Veblen and Burnham 1978). (e, f) Simulation and (g, h) atom filling structure
653 models showing the unit cell of Ftsk and Cjt with cation sites as marked (letters in legend correspond to those
654 used in Figure 1). The sites corresponding to *A* cavities in the amphibole are well-marked on the images and
655 simulations as the darkest, diamond-shaped motifs separating the octahedron strips. Paired-*A* cavities are
656 inferred for the triple-chain silicate considering the perfect fit between the simulation and the image in (b).
657 Likewise, the cations at the edges of the octahedron strip are attributable to ‘*B*’ sites.

658 **Figure 8.** *I-beam* models (digits refer to the number of chains in the silicate) as overlays on simulation (a) and
659 image (b) of amphibole with chain-width disorder displayed on [001] zone axis. Note the HAADF STEM
660 simulations and imaging provide a direct visualization of the intergrown structures since they show the main
661 building modules formed by the cations (compare with Figure 1 for the crystal models). (a) The single and
662 double zippers of triple-chain silicate within amphibole show coherent terminations along the zig-zag arrays of
663 cations at the edges of the octahedron strips. (b) The zippers are also readily depicted on the HAADF STEM
664 image by the longer octahedron strip and double-diamond shaped motifs typical of the triple-chain silicate.

665 **Figure 9.** HAADF STEM simulations (a, b) and images (c, d) showing relationships between *I-beam* models
666 (digits corresponding to the number of chains) and unit cells of ferro-tschermakite and clinojimbthompsonite
667 projected/imaged on [001] zone axis. (a, b) Two rows of *I-beam* stacks for the double- and triple-chain silicate
668 correspond to 1-, and 1.5-unit cells (white overlays), respectively. (c, d) Chain-width disorder in the Wirrda
669 Well amphibole is defined by single- and double-rows of triple-chain silicate. Note the mentioned 1- and 1.5-
670 unit cells correspond to lengths of ~ 27 Å and ~ 41 Å along the *b* axis, distances that include edges of $\frac{1}{2}$ unit
671 cells shared between the two pyriboles.

672 **Figure 10.** HAADF STEM images (a, b, d, e) and models (c, f, g) showing replacement of amphibole by
673 phyllosilicates and their intergrowths. (a) Irregular swells along the 3-chain silicate zippers in amphibole
674 (dashed line) imaged on [001] zone axis. (b) Detail of image in (a) showing the stepwise termination of a zipper
675 (arrowed). The distance of ~ 9.2 Å between alternating brighter and darker strips corresponds to the *c* parameter
676 of phyllosilicates such as a 2:1 mixture of pyrophyllite (P) and talc (T). (c) Replacement of 3-chain silicate by
677 phyllosilicates within the swell interpreted in terms of *I-beam* models whereby the (010) boundary between
678 phyllosilicates and amphibole (orientation in the inset) is coherent along the ‘**p** or **q**’ type slabs and gaps occur
679 at the zipper termination. (d) Chlorite (Chl) imaged on [100] zone axis displaying intergrowths with other
680 phyllosilicates. The FFT pattern (inset) shows the intergrowths are highly disordered along the *c** axis. (e)
681 Detail of image in (d; arrowed location) showing stacking disorder in chlorite. (f, g) Projection on [100] for
682 phyllosilicates used for interpreting the assemblages in (b) and (d). Crystal structure models from: [1]=Drits et
683 al. (2012); [2]=Zanazzi et al. (2007).

Table 1. Compositional data for tschermakite and ferro-tschermakite.

Conc. wt. %	Tsk (Mg-Hb)		Ferro-tschermakite		
	[1]	[2]	[3]	*[4]	
SiO ₂	45.90	40.12	41.32	44.28	
TiO ₂	0.44	0.87	0.37	0.57	
Al ₂ O ₃	14.43	18.67	18.13	18.33	
V ₂ O ₃			0.05		
Cr ₂ O ₃	1.73		0.02		
MnO	0.25	0.27	0.20	0.33	
FeO	2.79	16.75	17.55		
Fe ₂ O ₃	0.82	2.64		19.13	
NiO			0.01		
ZnO			0.02		
MgO	17.50	5.48	6.94	5.28	
CaO	11.98	11.65	10.58	10.50	
Na ₂ O	1.70	0.80	1.61	1.26	
K ₂ O	0.25	0.75	0.45	0.31	
H ₂ O ⁺	2.09	1.61	1.96		
F	0.10	0.07	0.12		
O=F,Cl (calc)	-0.04	-0.03	-0.05	0.00	
Total	99.94	99.65	99.28	100.0	
Recalculated wt. %					
FeO	1.02	17.16	14.72	16.91	
Fe ₂ O ₃	2.79	2.19	3.14	0.34	
H ₂ O ⁺	2.10	1.97	1.97	2.05	
Total	100.15	99.97	99.60	100.17	
a.p.f.u. calculated for 22 O atoms [calculations by spreadsheet of Locock et al. (2014)]					
<i>T</i>	Si	6.40	6.01	6.14	6.48
	Al	1.60	1.99	1.87	1.52
	ΣT	8.00	8.00	8.00	8.00
<i>C</i>	Ti	0.05	0.10	0.04	0.06
	Al	0.77	1.31	1.31	1.64
	V			0.01	
	Cr	0.19		0.00	
	Fe ³⁺	0.29	0.25	0.35	0.04
	Ni			0.00	
	Zn			0.00	
	Mn ²⁺				0.04
	Fe ²⁺	0.06	2.12	1.75	2.07
	Mg	3.64	1.22	1.54	1.15
ΣC	5	5	5	5	
<i>B</i>	Mn ²⁺	0.03	0.03	0.03	0.00
	Fe ²⁺	0.06	0.03	0.08	0.00
	Ca	1.79	1.87	1.68	1.65
	Na	0.13	0.07	0.22	0.35
ΣB	2	2	2	2	
<i>A</i>	Na	0.34	0.16	0.25	0.01
	K	0.04	0.14	0.09	0.06
	ΣA	0.38	0.31	0.33	0.07
ΣT,C,B,A	15.38	15.31	15.33	15.07	
<i>W</i>	OH	1.96	1.97	1.94	2
	F	0.04	0.03	0.06	
ΣW	2	2	2	2	

Abbreviations: Tsk=tschermakite; (Mg-Hb=magnesiohornblende. [1] Abdu and Hawthorne (2009); [2] Hawthorne and Grundy (1973); [3] Oberti et al. (2018); [4] Wirrda Well, present study. *= mean of integrated area using Schreiber-Wims and Brown-Powell methods.

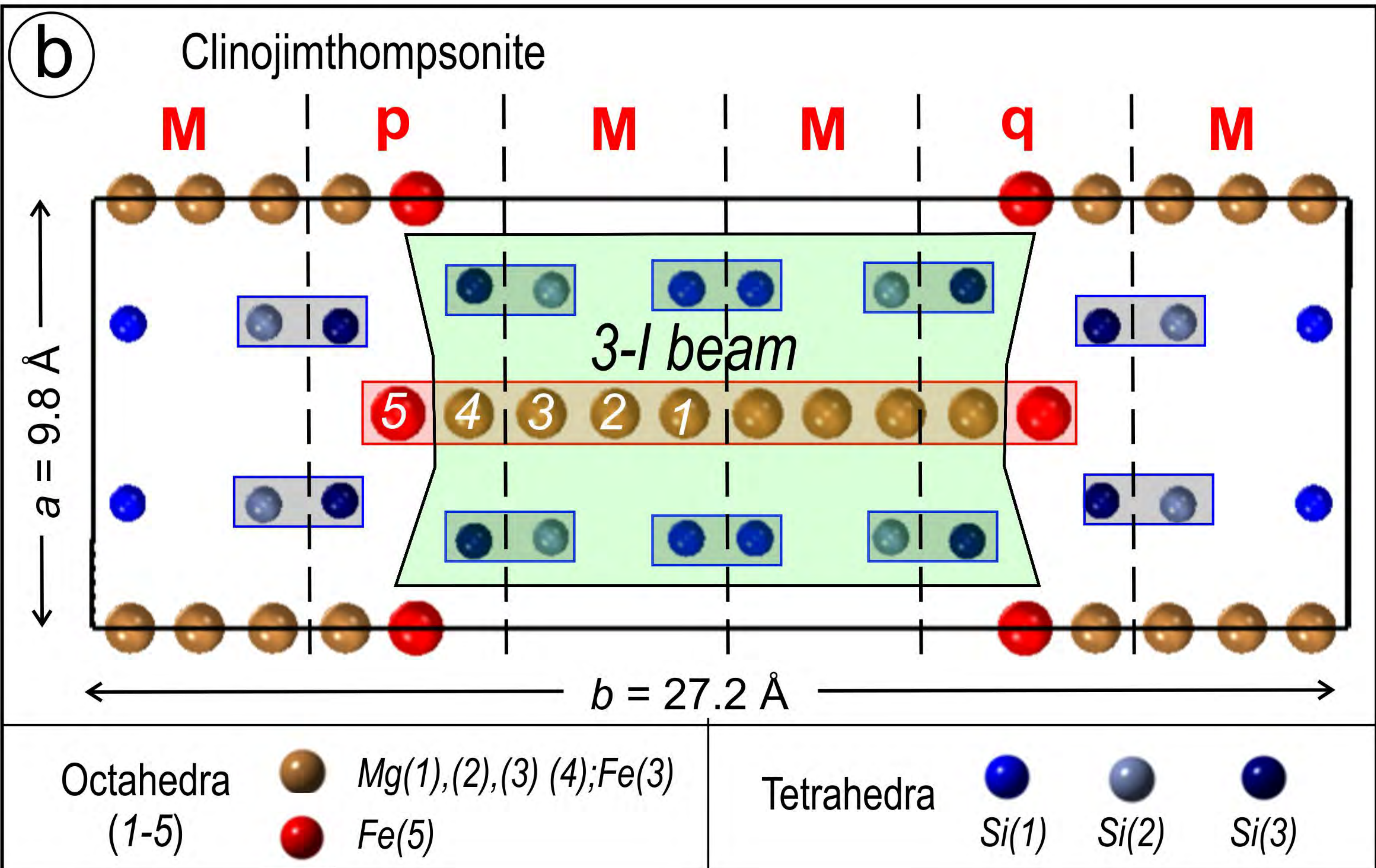
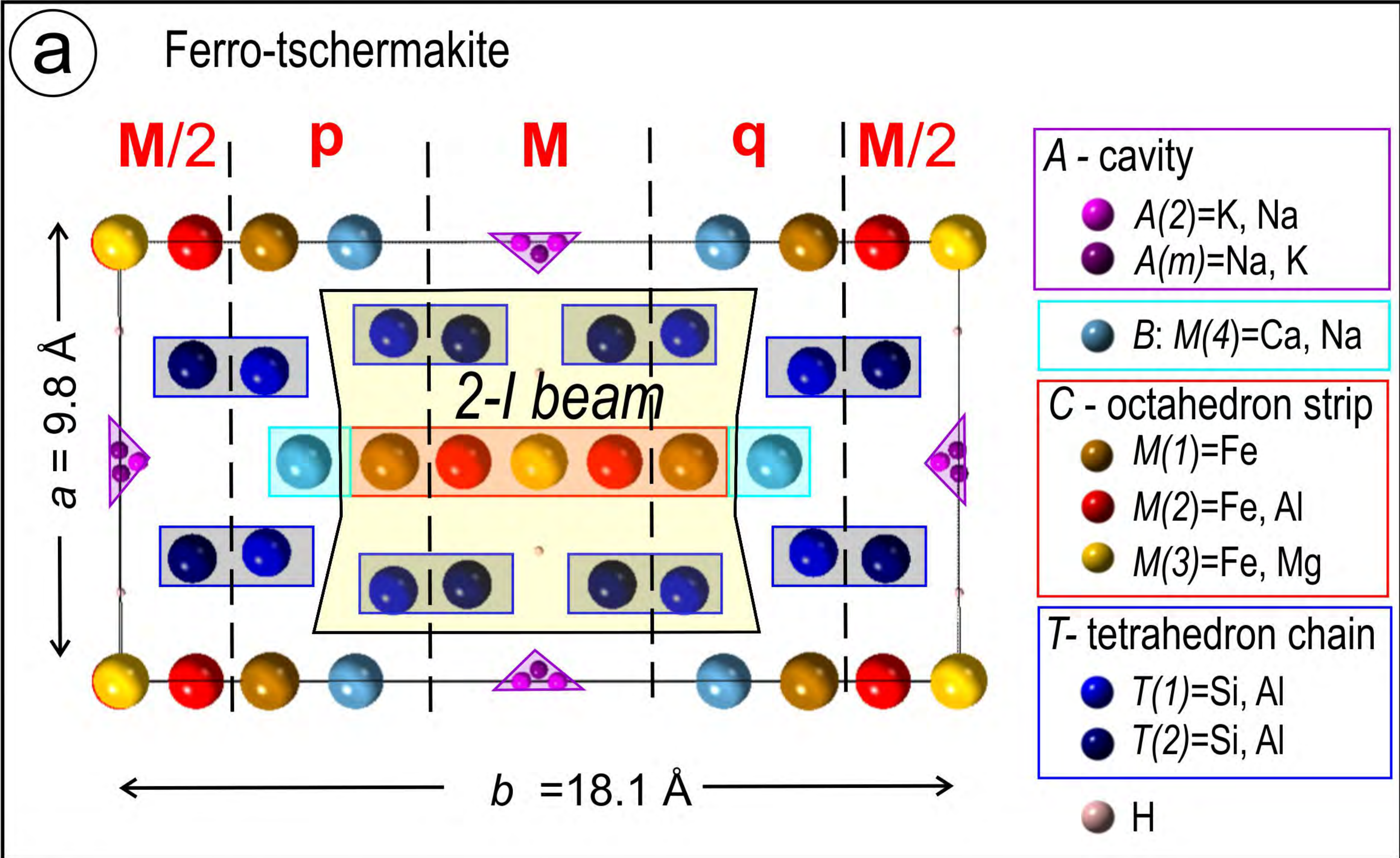


Figure 1

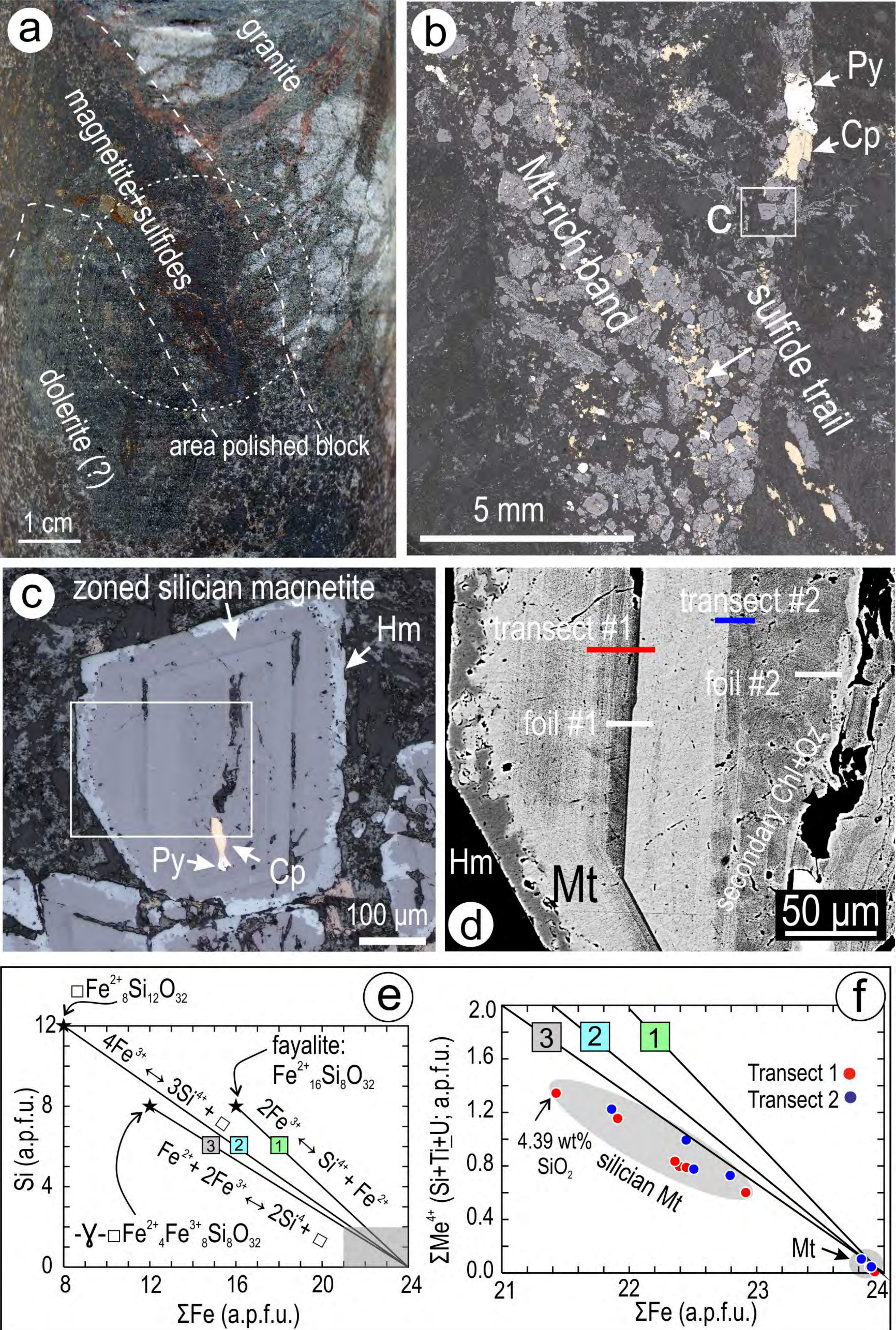


Figure 2

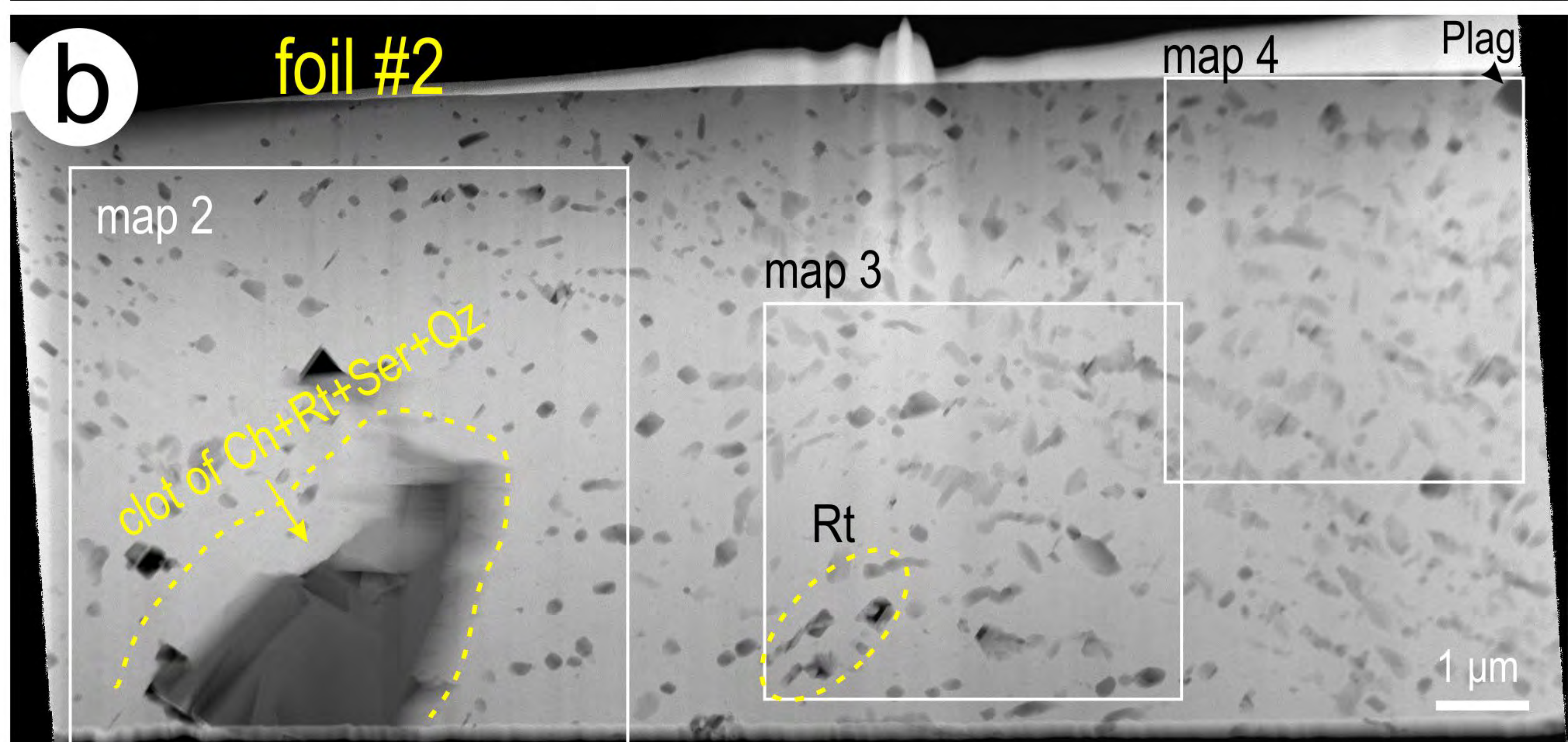
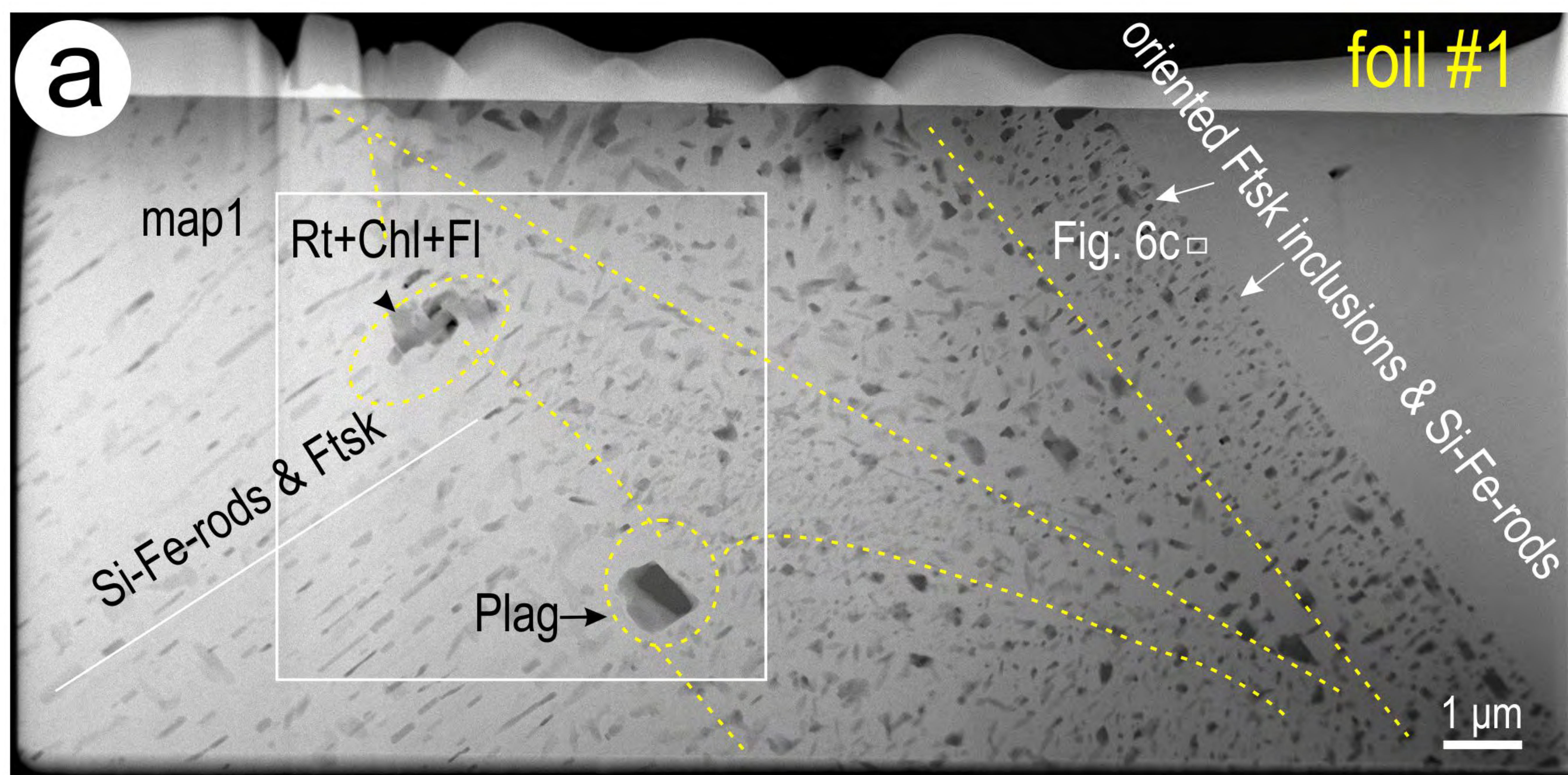
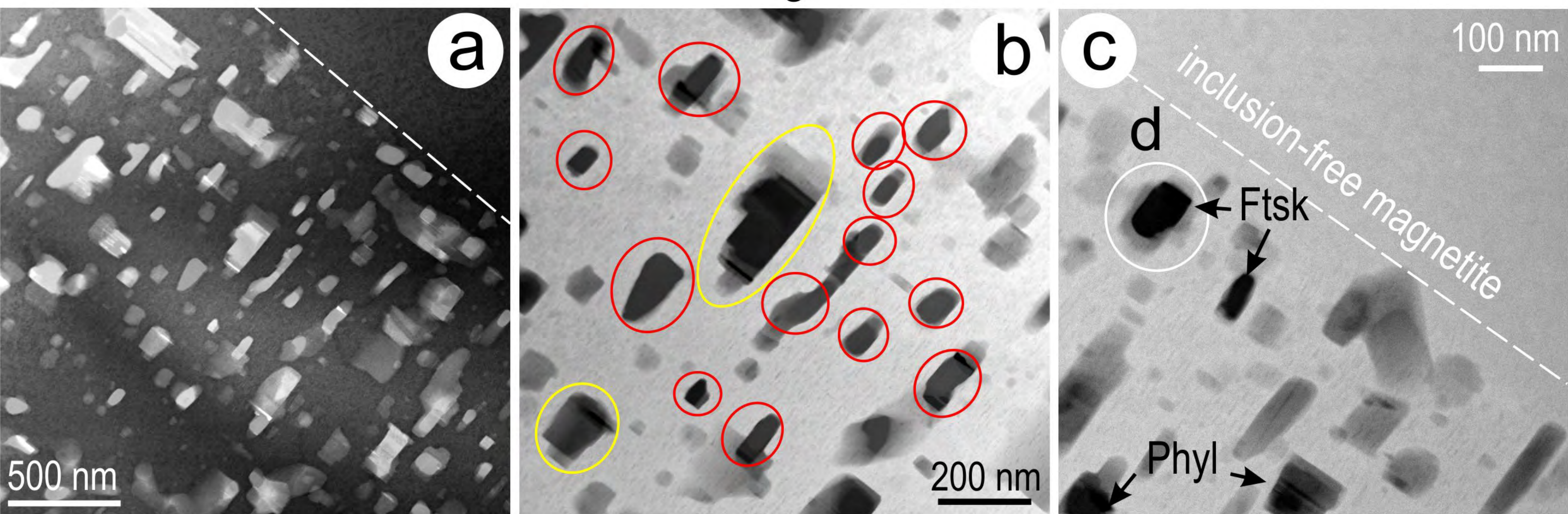
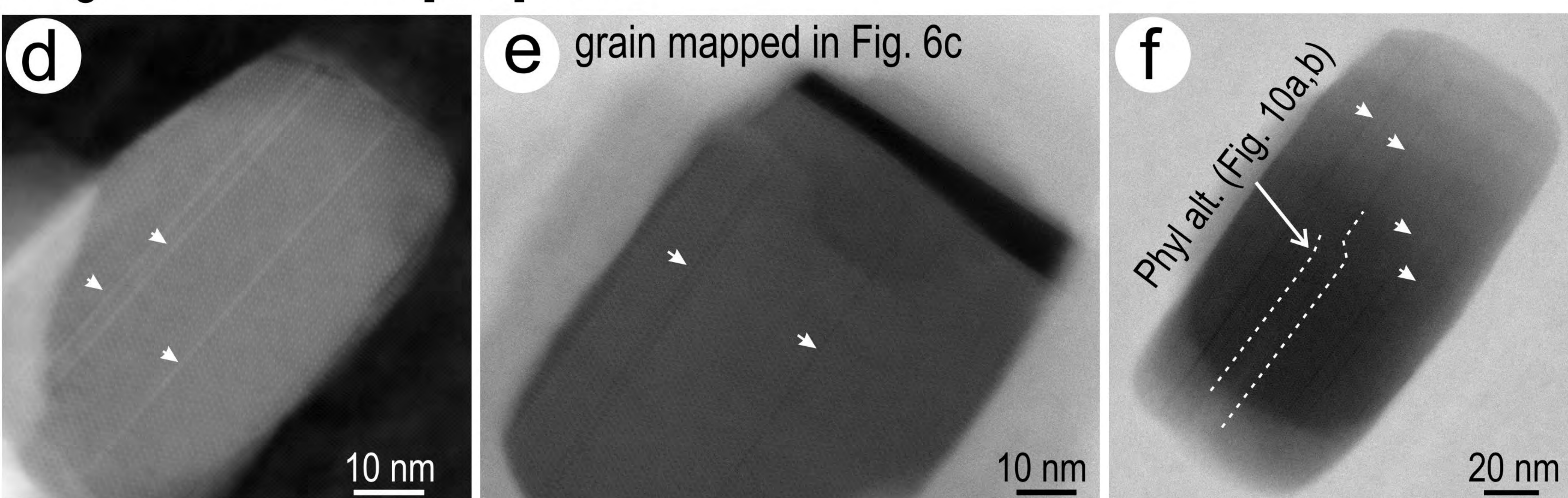


Figure 3

BF (a) and HAADF STEM (b, c) images of the boundary between inclusion-rich and -free zones in magnetite



BF (d) and HAADF STEM (e, f) images of ferro-tschermakite grains in magnetite tilted on $[11\bar{2}]$ zone axis



HAADF STEM images of phyllosilicate lamellar aggregates in magnetite

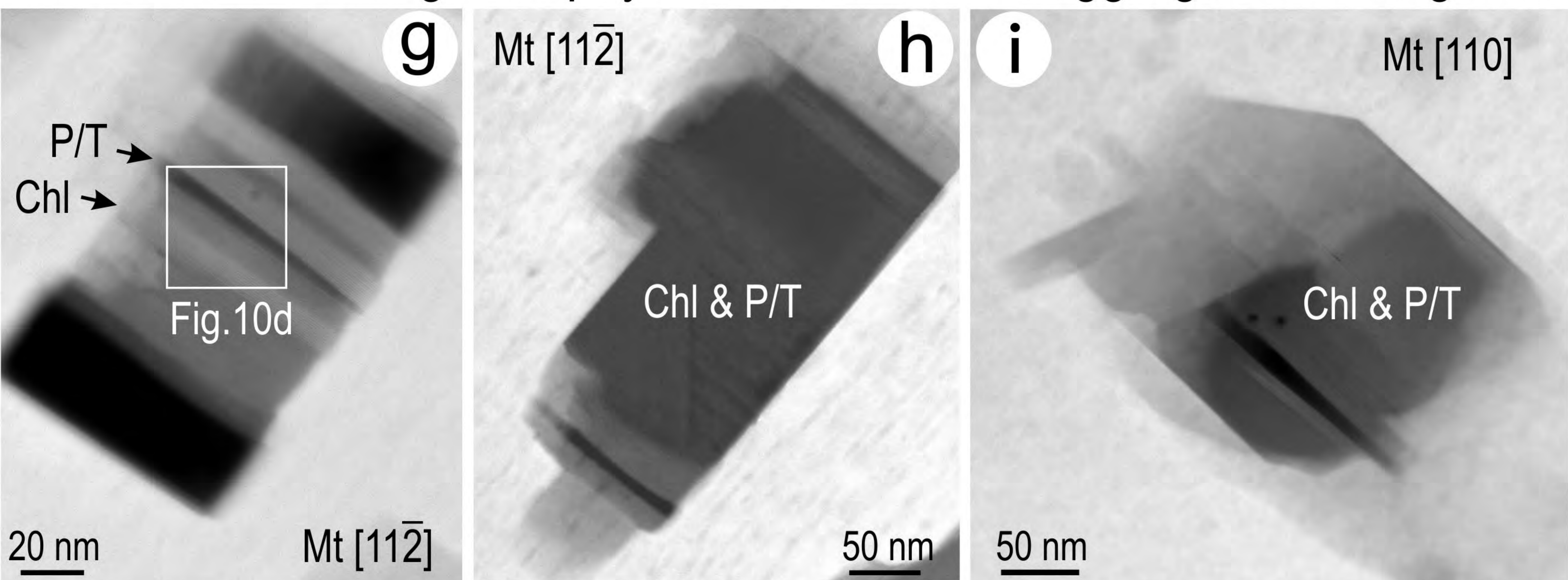


Figure 4

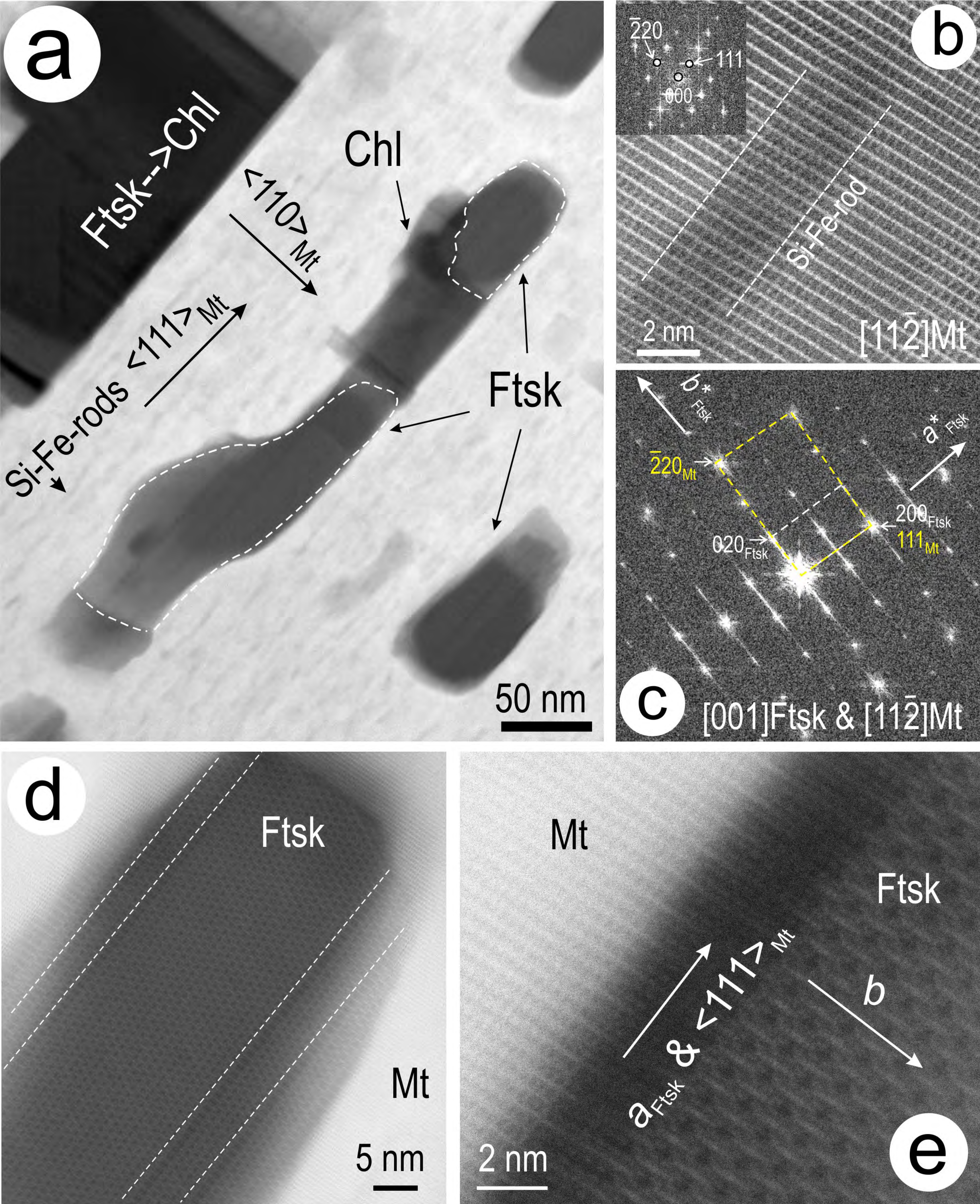


Figure 5

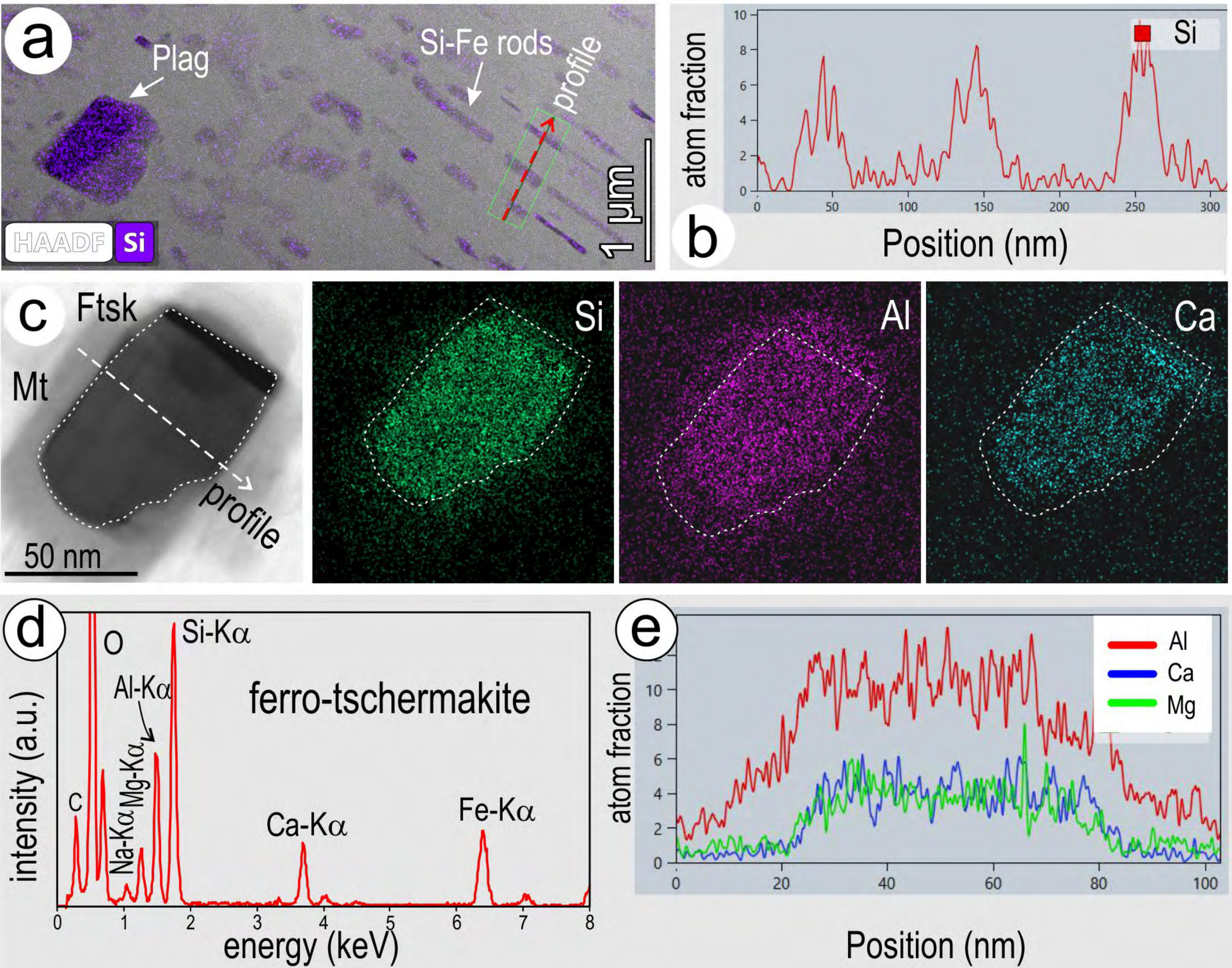


Figure 6

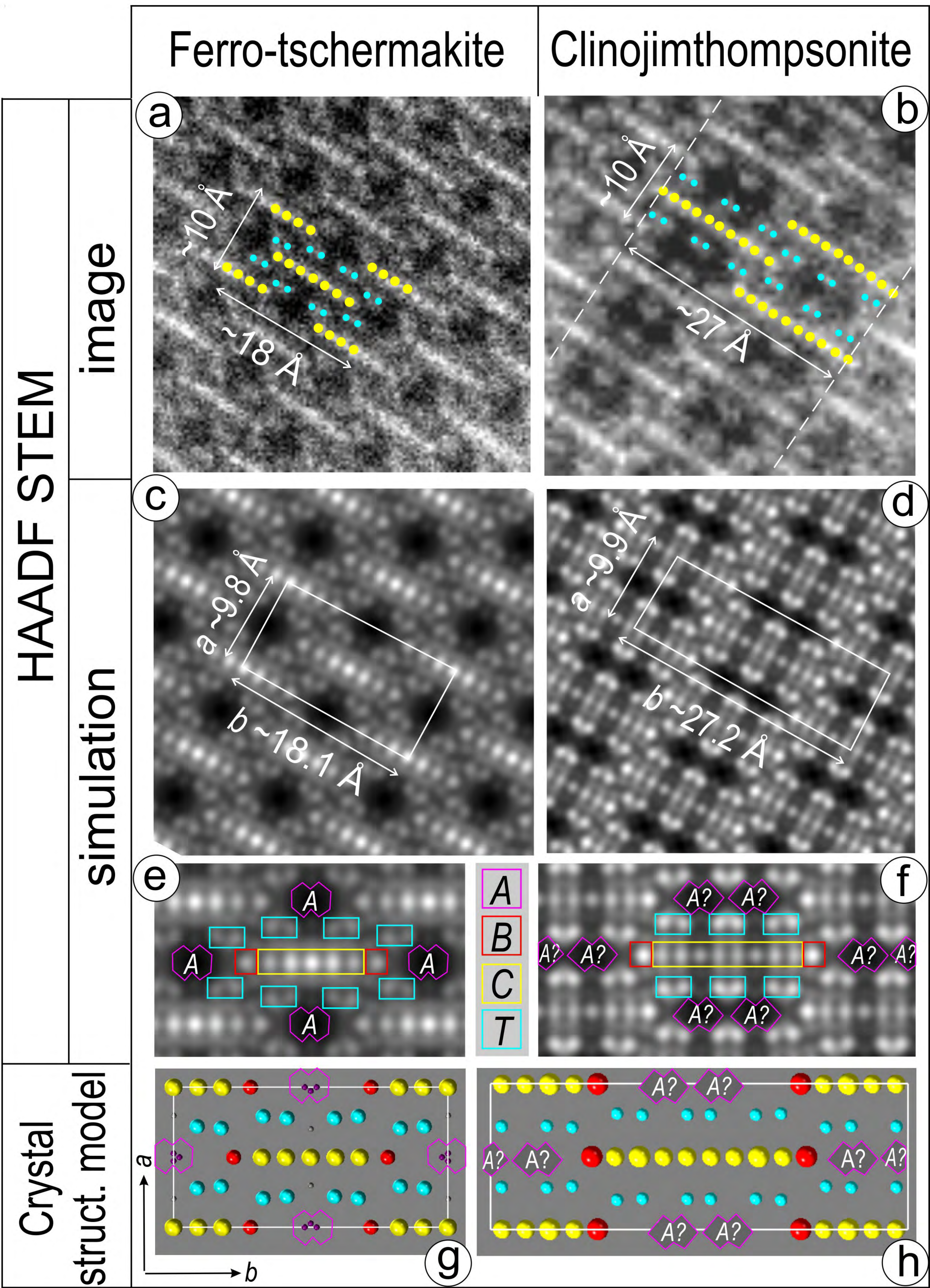


Figure 7

HAADF STEM

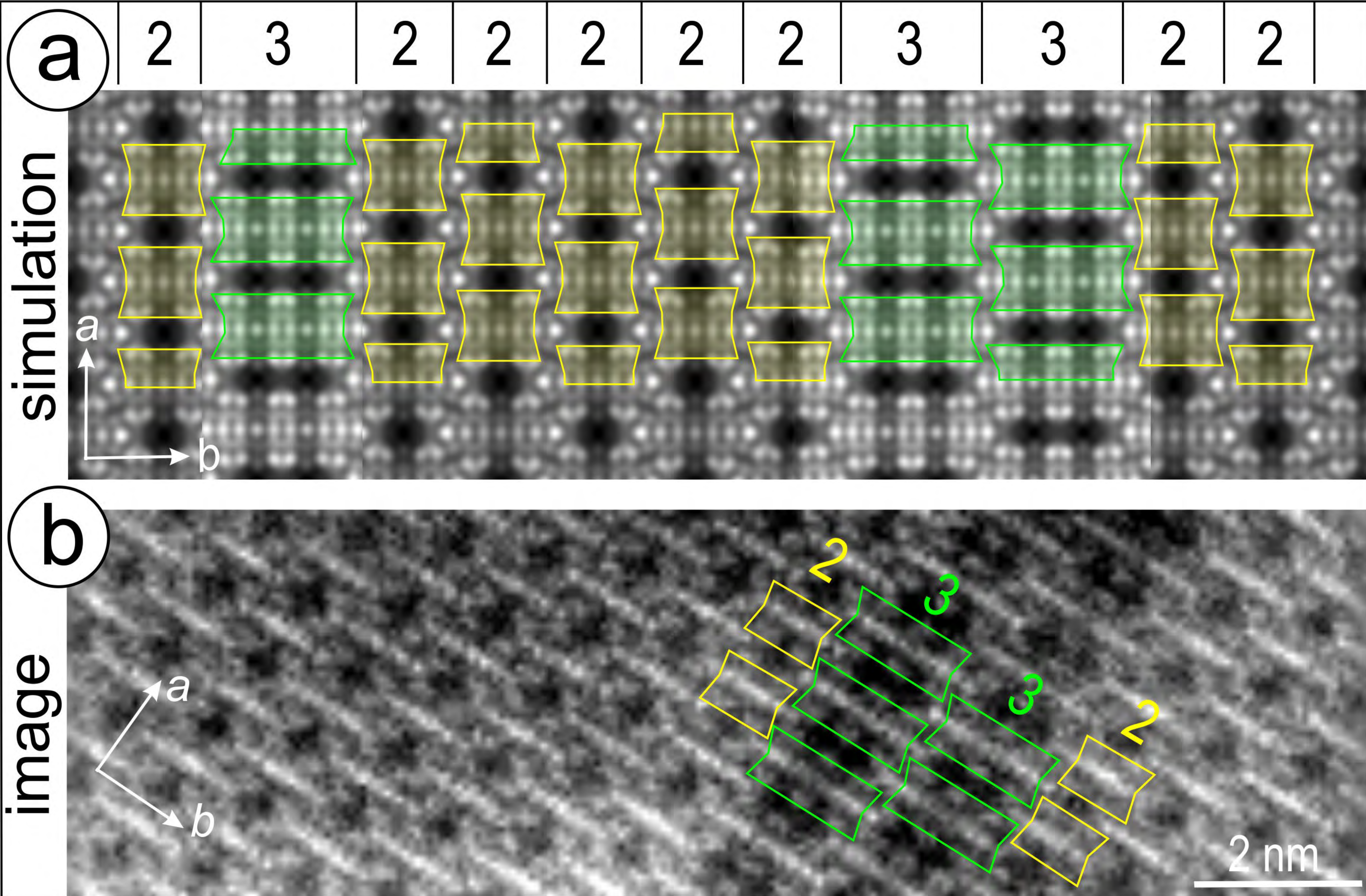
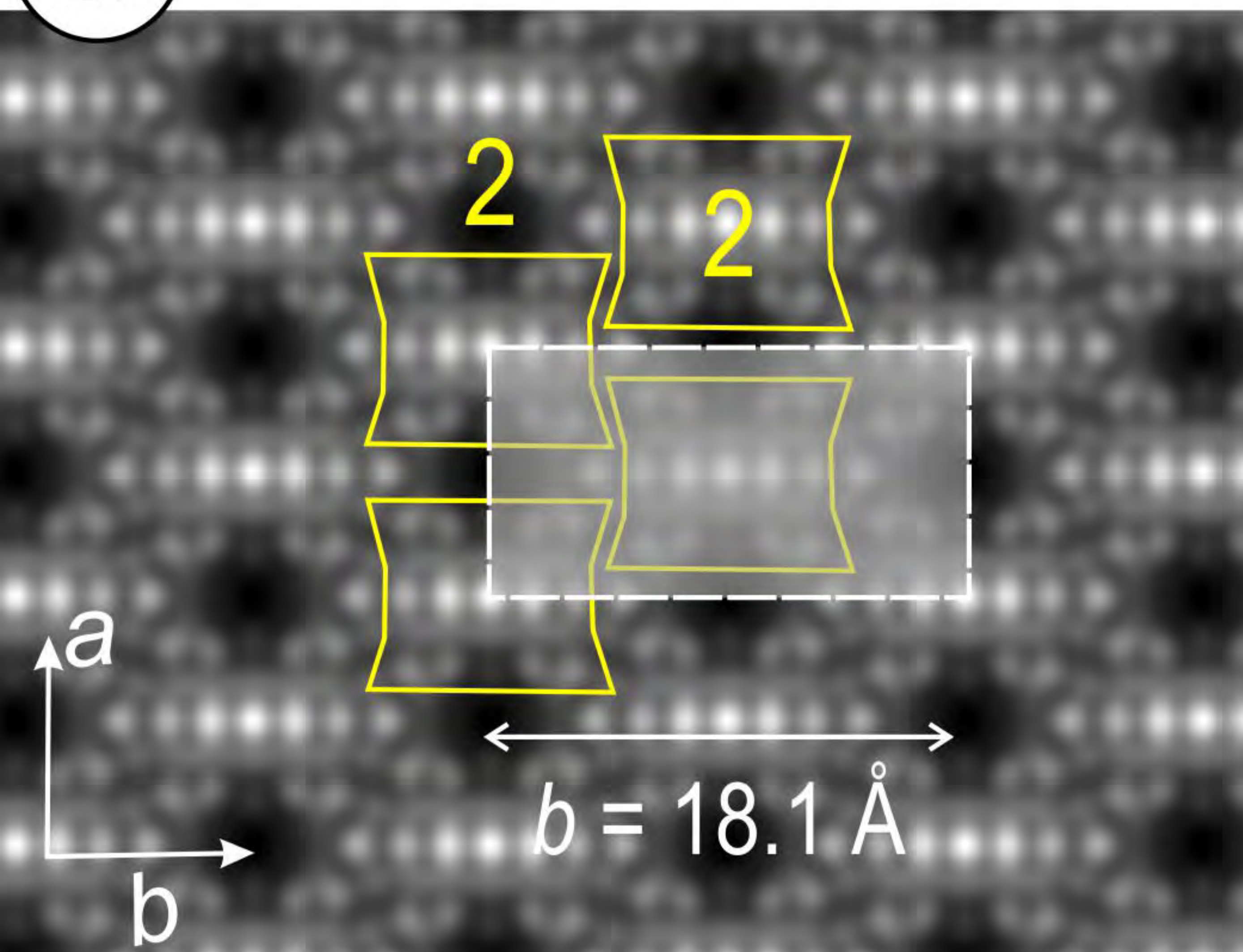


Figure 8

a Ferro-tschermakite



b Clinojimthompsonite

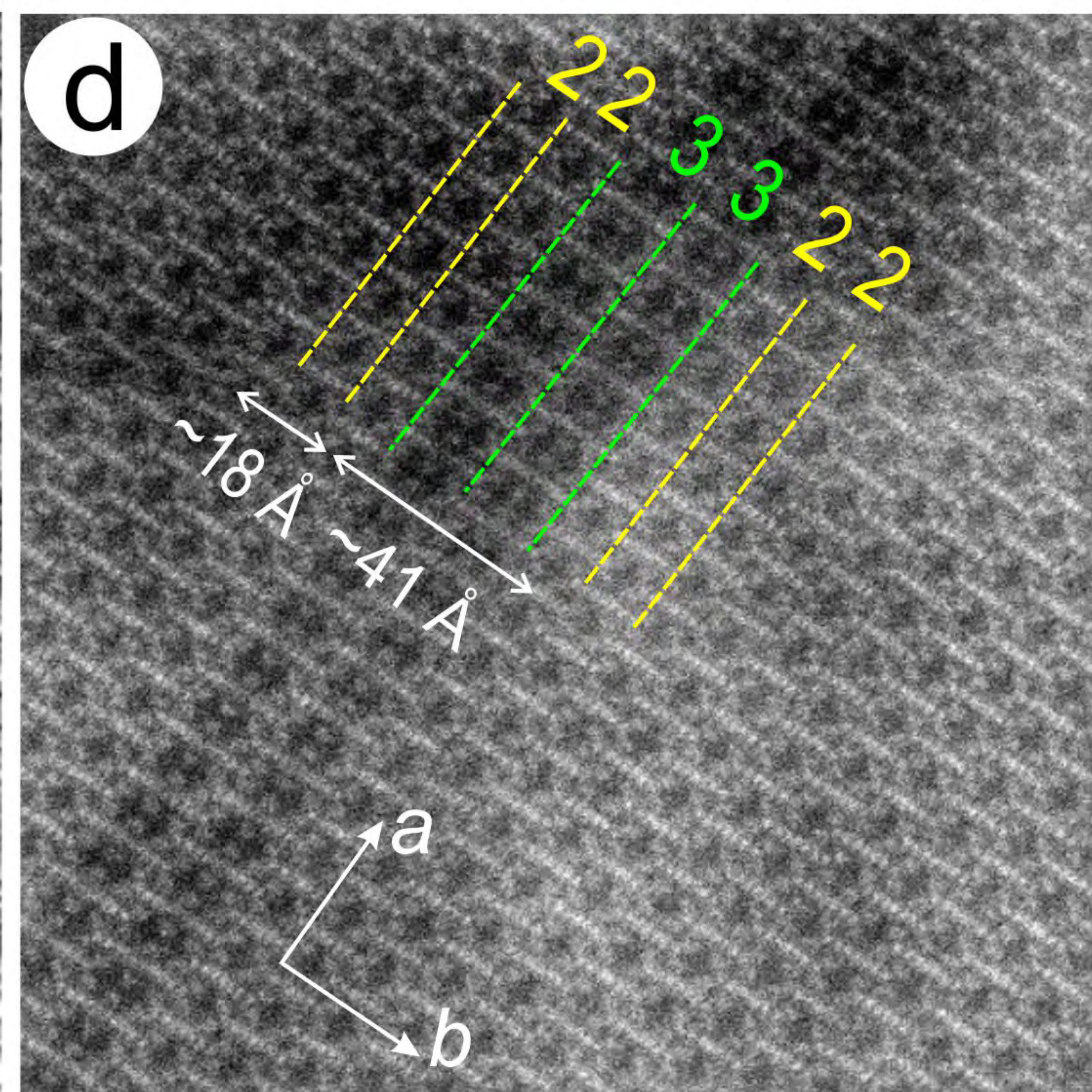
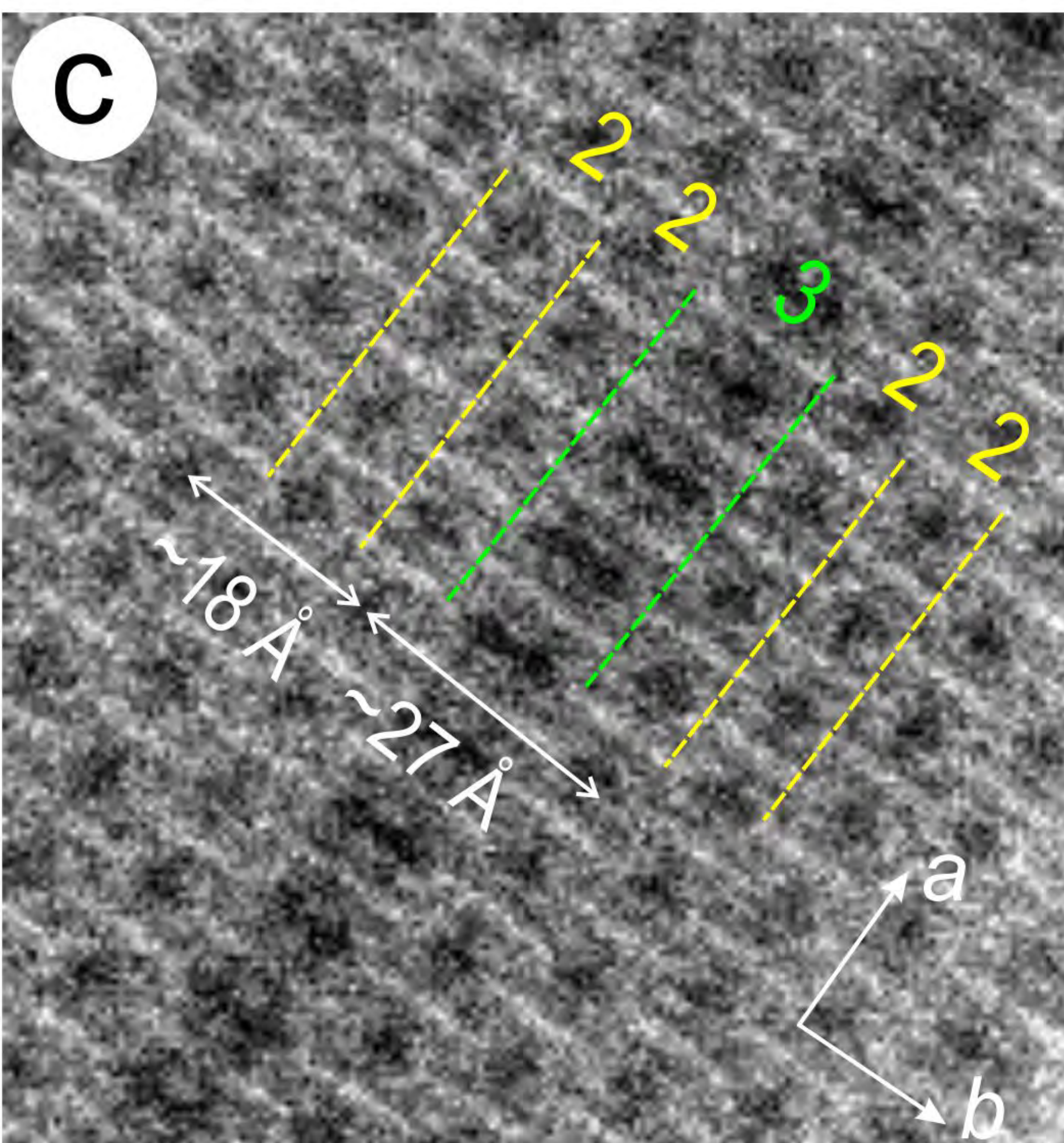
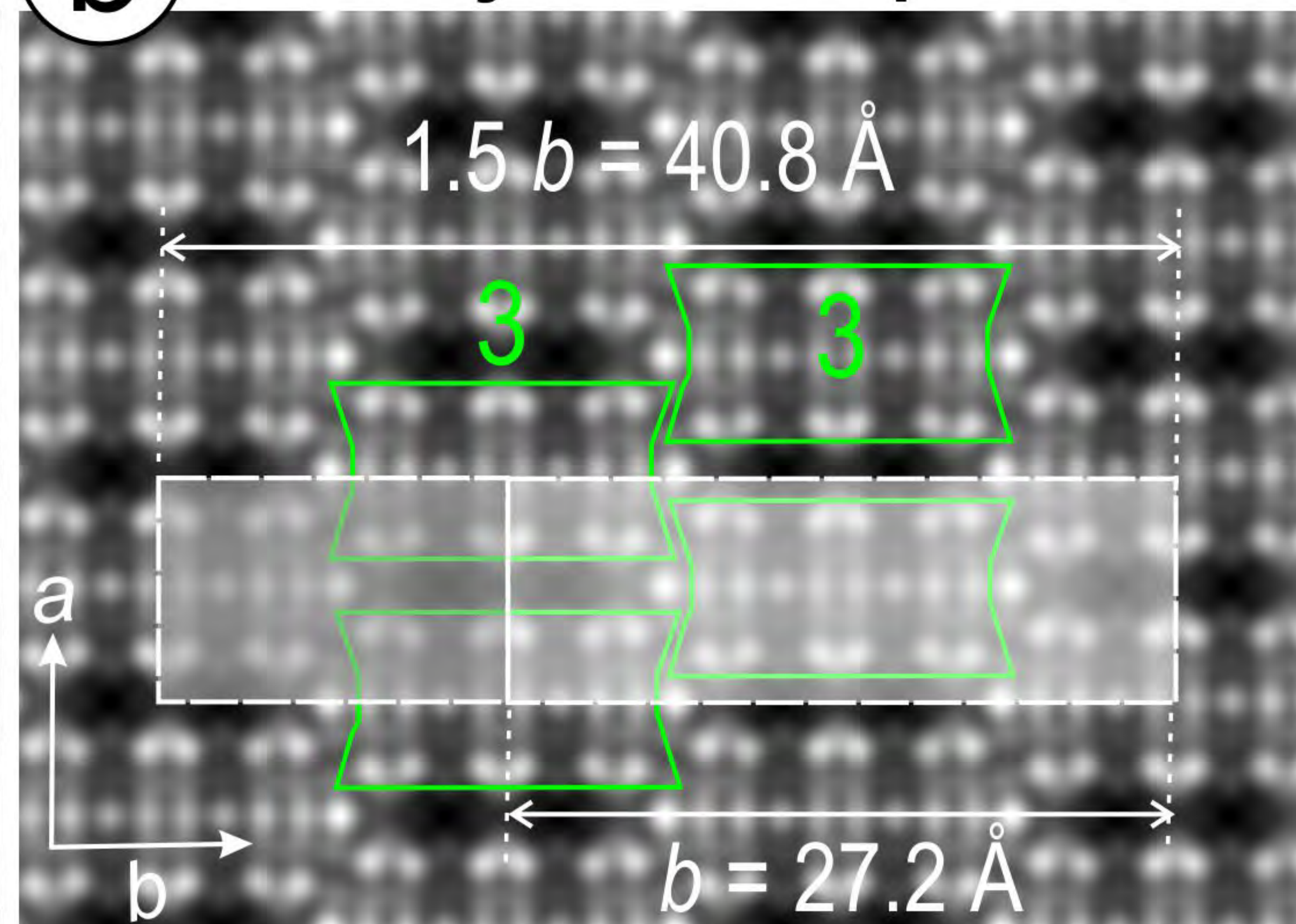


Figure 9

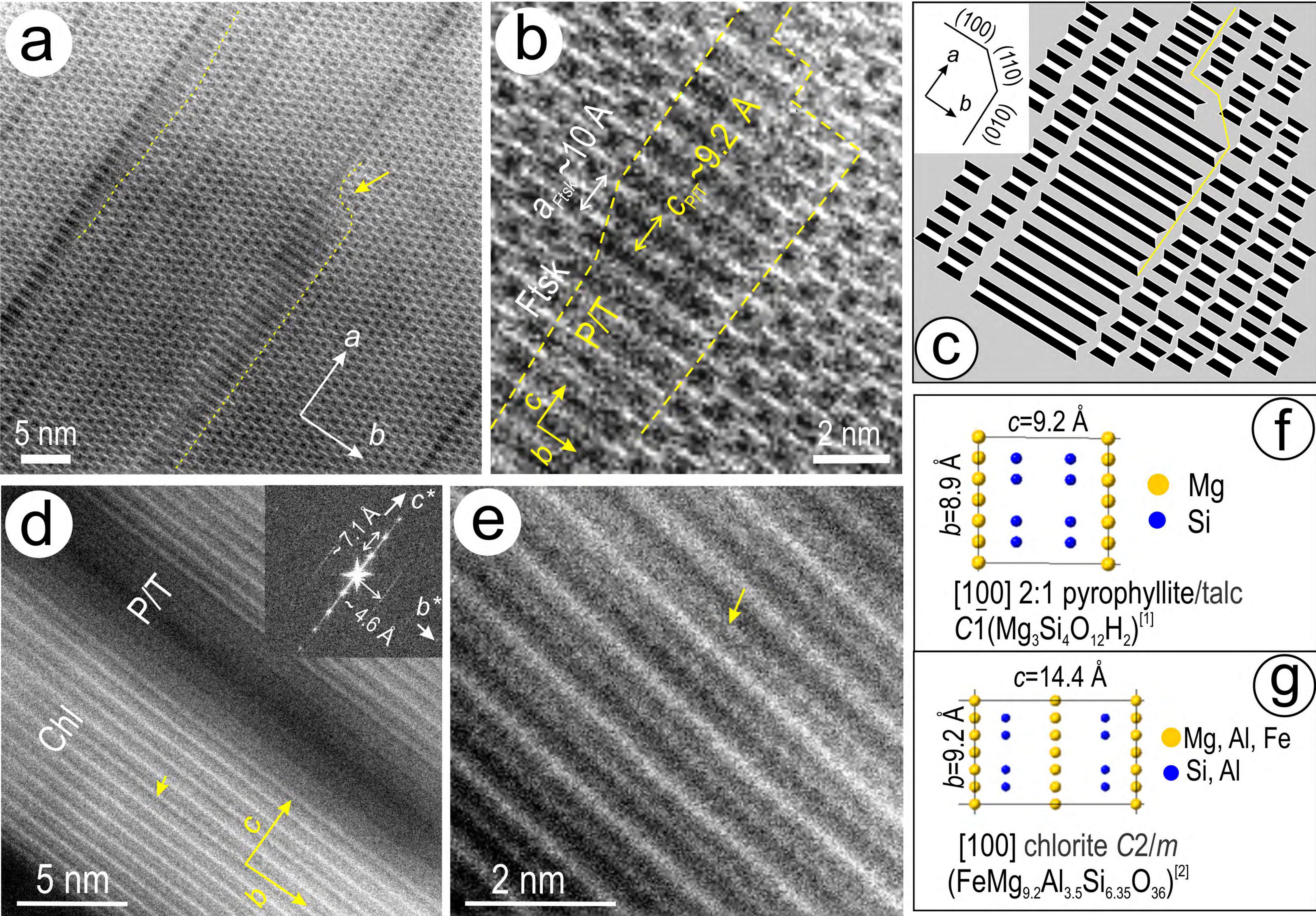


Figure 10